BM13.1-ĐT-BVCS

BỘ GIÁO DỤC & ĐÀO TẠO
TRƯỜNG ĐẠI HỌC SƯ PHẠM KỸ THUẬT THÀNH PHỐ HỒ CHÍ MINH

CỘNG HÒA XÃ HỘI CHỦ NGHĨA VIỆT NAM
Độc lập - Tự do - Hạnh phúc

TÓM TẮT NHỮNG ĐÓNG GÓP MỚI CỦA LUẬN ÁN

Họ & tên NCS: Phan Thị Đăng Thư. MSNCS: 13252010305

Thuộc chuyên ngành: Kỹ thuật cơ khí. Khoá: 2013 - 2016

Tên luận án: Buckling Analysis of Inflatable Composite Beams

Người hướng dẫn chính: PGS.TS Phan Đình Huấn

Người hướng dẫn phụ: PGS.TS Lê Hiếu Giang

Tóm tắt những đóng góp mới về lý luận và học thuật của luận án:

Luận án này có những đóng góp mới như sau:

- Tham khảo, tìm hiểu, tổng hợp các mô hình tính tải tới hạn cho kết cấu dầm hơi vật liệu vải dệt composite để chọn ra mô hình thích hợp cho các phương trình giải tích và mô hình tính phần tử hữu hạn. Mục tiêu của phần này là để có thêm công cụ giải tích và công cụ phần tử hữu hạn truyền thống nhằm kiểm chứng kết quả tính IGA và kết quả thực nghiệm của luận án.

- Nghiên cứu áp dụng công cụ tính số "đẳng hình học- IGA" để xác định tải tới hạn cho kết cấu dầm hơi vật liệu vải dệt composite với các điều kiện biên khác nhau. Một đoạn code bằng MatLAB cũng được phát triển.

- Nghiên cứu thực nghiệm nhằm:

+ Xác định các hằng số vật liệu vải dệt composite. Các hằng số này dùng để làm dữ liệu đầu vào cho các chương trình tính.

+ Thiết lập các thí nghiệm về dầm bơm hơi trong điều kiện thiết bị và vật tư có thể tìm trong nước và mua của nước ngoài.

+ Xác định tải tới hạn của kết cấu dầm hơi vật liệu vải dệt composite với các điều kiện biên khác nhau.

+ Khảo sát ảnh hưởng của áp suất hơi ban đầu (áp suất trong) đến độ bền của dầm hơi.

+ Khảo sát ảnh hưởng của áp suất hơi ban đầu (áp suất trong) đến tải tới hạn gây mất ổn định của kết cấu dầm hơi.

- Trên cơ sở tổng kết các nội dung đã thực hiện của luận án, các hướng nghiên cứu tiếp theo được đề xuất.

- Các đóng góp mới của luận án có thể ứng dụng trong lãnh vực đào tạo và trong thực tế sản xuất.

Tp. Hồ Chí Minh, ngày tháng năm 2021

Nghiên cứu sinh

Phan Thị Đăng Thư

Người hướng dẫn chính	**Người hướng dẫn phụ**
(*Ký và ghi rõ họ tên)*	*(Ký và ghi rõ họ tên)*
PGS. TS. Phan Đình Huấn	**PGS. TS. Lê Hiếu Giang**

BM13.2-ĐT-BVCS

MINISTRY OF EDUCATION AND TRAINING
HO CHI MINH CITY UNIVERSITY OF TECHNOLOGY AND EDUCATION

THE SOCIALIST REPUBLIC OF VIETNAM
Independence – Freedom - Happiness

SUMMARY OF CONTRIBUTIONS OF THE DISSERTATION

PhD candidate:	Phan Thi Dang Thu	Fellows code: 13252010305
Major:	Mechanical Engineer	Major code: 2013 – 2016
Dissertation title:	Buckling Analysis of Inflatable Composite Beams	
Supervisor one:	Assoc. Prof.Dr Phan Dinh Huan	
Supervisor two:	Assoc. Prof.Dr Le Hieu Giang	

Summary of theoretical and academic contribution of the dissertation:

This thesis has the following new contributions:

- Refer, study and synthesize critical load calculation models for inflatable beam structures of composite textiles to choose a suitable model for analytical equations and finite element calculation models. The goal of this section is to have more analytical tools and traditional finite element tools to verify the IGA calculation results and the experimental results of the thesis.

- Applying the "isogeometric Analysis- IGA" numerical computation to determine the critical load for the composite woven fabric's inflatable beam structure with different boundary conditions. A piece of code in MatLAB was also developed.

- Experimental research to:

+ Determine textile composite material constants. These constants are used as input data for calculation programs.

+ Set up experiments on inflatable beams in terms of equipments and supplies that can be found locally and purchased from abroad.

+ Determine critical load of steam beam structures of composite textile materials with different boundary conditions.

+ Investigate the effect of initial internal pressure on the strength of the inflatable beam.

+ Investigate the effect of initial internal pressure on critical load causing buckling of inflatable beam structure.

- Based on summary of the done contents of the thesis, next research works are proposed.

- The new contributions of this thesis can be applied in the field of training and in production industry.

HCMC, / /2021
PhD candidate
(Sign and name)

Phan Thi Dang Thu

Supervisor 1
(Sign and name)

Assoc. Prof. PhD. Phan Dinh Huan

Supervisor 2
(Sign and name)

Assoc. Prof. PhD. Le Hieu Giang

MINISTRY OF EDUCATION AND TRAINING

HCM CITY UNIVERSITY OF TECHNOLOGY AND EDUCATION

---oo0oo---

PHAN THI DANG THU

BUCKLING ANALYSIS OF INFLATABLE COMPOSITE BEAMS

MAJOR: MECHANICAL ENGINEERING

CODE: 62520103

PHD THESIS SUMMARY

HCM city, November 2020

ABSTRACT

This thesis presents an experimental program and numerical modeling for buckling behavior of inflatable beams made from woven fabric composite materials. In the experiment study, the mechanical properties of the woven fabric composite material used in frabrication of inflatable beams are determined and the biaxial buckling test is carried out. In the numerical study, isogeometric analysis (IGA) is utilized to analyze the bucking response of inflatable beams subject to axial compressive load and predict the critical load at which the first wrinkle occurs. The numerical modelling is then calibrated with the experiments. A good agreement between IGA predictions and test results is achieved.

First of all, Timoshenko's kinematics principle is used to build a 3D model of inflating orthotropic beam. In this modeling process, non-linearity is considerated. By using Lagrangian and virtual work principles, nonlinear equilibrium equations were derived and determined. These equations are then linearized, and their results regulated the linearized equations. Therefore, analytical expressions of vital buckling load are obtained based on the linearized equations.

Secondly, the stability analysis of a homogeneous orthotropic woven fabric inflating beam is based on the IGA. In this analysis, a quadratic NURBS-based Timoshenko element of beam with C1-type continuity is applied. The formula of element is constructed by using the energy concept that accounts for the change in membrane and strain energies as the beam is bent. The results constructed stiffness matrix of the beam.

Thirdly, the experimental studies are performed under various inflation pressures to characterize the orthotropic mechanical properties and the nonlinear buckling behaviors. The experimental results help to monitor the initiation of the first wrinkles of the beam. Also, the critical buckling load is determined through distinct load cases. The discrepancy is evaluated among the proposed orthotropic and isotropic models in literature.

Aditionally, the the experimental results found that the load versus deflection curve of inflatable beams are illustrated. The buckling behaviour of the orthogonal fibre-laminated fabrics beam was determined. The load versus displacement relation of the inflatable beam with different air pressures was discovered. The maximum load carrying capacity of the inflatable beam with respect to the appearance of the first wrinkle was found.

GENERAL INTRODUCTION

1. Domestic researches

The inflatable structures are common structures which are currently used in amusing and performing projects, such as buoy houses in children's play areas, welcome gate, animals images, etc. In Vietnam, the inflatable structures are a relatively new field. Currently, designing and analyzing of the inflatable structures for big projects have been facing difficult challenges.

Nowadays, some research teams are studying the applications of inflatable structures. Particularly, Le et al. presented the inflatable structures application to build air-cushion running ships (On the Air Cushion Model for a Hovercraft with Flexible Skirts, Transportation Science and Technology Journal (ISSN1859-4263). However, they only focuse on the geometrical design to optimize air source for the air-cushion running ships.

2. Foreign researches

In recent decades, there has been plenty of studies on beams, sheets and pipes structures made of inflatable. These inflatable structures are concentrated by some papers as follows.

2.1 The main investigation about theoretical approach

Many analytical techniques have been already made on inflatable beams. Generally, the beams were supposed to be made from a homogeneous isotropic fabric and the usual Saint Venant Kirchhoff hypothesis was used.

Besides, disparate authors have also applied Euler Bernoulli's kinematics. For example, load deflection theory was derived Comer and Levy (1963) for an inflating isotropic beam by using the usual Euler Bernoulli's kinematics. After that, Comer and Levy's work was extended by Webber (1982) to predict distructing loads in cantilever beams that was inflating. Also, Main et al. (1995s) did experiments on a cantilever isotropic beam and then Comer's theory was improved typically. Continuously, Suhey et al. (2005) considered a tube pressurized under uniformly distributed loads. By the means of the Euler-Bernoulli's kinematics, material of beams was supposed to be isotropic and their results was obtained theoreticaly for deflection.

In addition, the Timoshenko's kinematics is determined by some other authors have that it is the best adapted theory for structures as pressure load does not appear in solution of deflection, which is mentioned in the Euler Bernoulli's kinematics situation. For instance, a seri of nonlinear equations was derived by Fichter (1966) for the bending and twisting of inflating cylindrical beams. This derivation was based on three following significant assumptions: cross section of the inflating beam, which is the first issue, remains undeformed under the applied loading; secondly, the cross-sectional translation and rotations are small; and the negligible characteristic of circumferential strain is the third assumption. He used the Timoshenko kinematics and energy minimization approach. A homogeneous isotropic fabric is supposed to

apply on the beam. Later Topping (1963) and Douglas (1969) have investigated the structural stiffness of an inflating cylindrical cantilever beam that was influenced by large deformations. The finite theory of elasticity and the theory of small deformations have been employed to obtain explicit analytical results. Their analyses also account for the changes of geometry and material properties that occur during the inflation process.

In the recent decades, Wielgosz and Thomas (2002) have derived analytical solutions for inflating panels and tubes by using the Timoshenko kinematics and by writing the equilibrium equations in the deformed state of the isotropic beam in order to take into account the geometrical stiffness and the follower force effect due to the internal pressure. They have shown that the limit load is proportional to the applied pressure and that the deflections are inversely proportional to the material properties of the fabrics and to the applied pressure.

Thomas (2002) and Thomas and Wielgosz (2004) have presented experimental, analytical and numerical results on the deflections of highly inflating fabric tubes submitted to bending loads. Experiments have been displayed and they have shown that the tube behaviour looks like that of inflating panels. Equilibrium equations have been once again written in the deformed state to take into account the geometrical stiffness and the follower forces. Comparisons between experimental and analy tical results have proven the accuracy of their beam theory for solving problems on the deflections of highly inflating tubes.

Le and Wielgosz (2005) have used the virtual work principle in Lagrangian form and the usual Saint Venant Kirchhoff hypothesis with finite displacements and rotations in order to derive the nonlinear equations for inflating isotropic beams. The nonlinear equilibrium equations have been linearized around the pre-stressed reference configuration which has to be defined as opposed to the so-called natural state. These linearized equations have improved Fichter's theory.

Although a lot of research groups have made much efforts in developing the analytical methods over many years but almosts they have focused on isotropic fabric materials. Until now, there has a little work that focuses on the case of orthotropic fabric material.

2.2 The main investigation about numerical approach

Nowadays, inflatable beams pose significant challenges to the analysts. In the numerical modelling of inflatable beams, significant prior researches have been conducted. Steeves (1975a, b) has used the principle of minimum potential energy to derive a set of governing differential equations for lateral deformation of inflated beams. A simplifying approximation, assuming that the cross sections of the beam remain undeformed, has then been employed to reduce the dimensions to one dimension: This beam element has included a pressure stiffening term. Quigley et al. (2003) and Cavallaro et al. (2003) have used this finite element to predict the linear load-deformation response of inflated fabric beams. However, the pressure stiffening term in Steeves's element has treated the axial pressure resultant as an externally applied stiffening tension force. This formulation has predicted an unbounded increase in beam stiffness with increasing inflation pressure.

Wielgosz and Thomas (2002, 2003) and Thomas and Wielgosz (2004) have studied the load-deflection behaviour of highly inflated fabric tubes and panels, and have developed a specialized beam finite element using Timoshenko beam theory. In their approach, the force generated by the internal pressure has beeen treated as a follower force which has accounted for pressure stiffening effects. However, the element formulation did not consider the fabric wrinkling.

Bouzidi et al. (2003) have presented theoretical and numerical developments of finite elements for azisymmetric and cylindrical bending problems of pressurized isotropic membranes. The external loading has been mainly a normal pressure to the membrane and the developments have been made under the assumptions of follower forces, large displacements and finite strains. The total potential energy has been minimized, and the numerical solution has been obtained by using an optimization algorithm.

Suhey et al. (2005) have presented a numerical simulation and design of an inflatable open-ocean-aquaculture cage using nonlinear finite element analysis of isotropic membrane structures. Numerical instability caused by the tension-only membrane has been removed by adding an artificial shell with small stiffness. The finite element model has been compared with a modified beam theory for the inflatable structure. A good agreement has been observed between the numerical and theoretical results.

Le and Wielgosz (2007) have discretized the nonlinear equations obtained in Le and Wielgosz (2005) to carry out a finite element formulation for linearized problems of highly inflated isotropic fabric beams. Their numerical results obtained with the beam element have been shown to be close to their 3D isotropic fabric membrane finite element and analytical results obtained in Le and Wielgosz. (2005).

Davids (2007) and Davids and Zhang (2008) have derived a Timoshenko beam finite element for nonlinear load-deflection analysis of pressurized isotropic fabric beams and the numerical examination of the effect of pressure on the beam loaddeflection behaviour. The basis of their element formulation has been an incremental virtual work ezpression that has included explicitly the work done by the pressure. Parametric studies have been also investigated to demonstrate the importance of including the work done by the pressure in their models.

More recently, Malm et al. (2009) have used 3D isotropic fabric membrane finite element model to predict the beam load-deformation response. Comparison between the finite element model load-deflection responss and beam theory has shown the accuracy of the conventional beam theory for modelling the isotropic fabric airbeam. Most of the former works, the fabric was always supposed to be isotropic.

Considering the inflatable beams made of orthotropic fabric materials, several research groups have been conducted. Plaut et al. (2000) have studied the effect of the snow and wind loads on an inflated arch in the assumption of linear thin-shell theory of Sanders. They have used this theory to formulate the governing equations, which include the effect of the initial membrane stresses. The material was assumed to have a linearly elastic, nonhomogeneous and orthotropic behaviour. Approzimate

solutions have been obtained using the Rayleigh-Ritz method. Plagiannakos et al. (2009) have studied a low pressure Tensairity in order to estimate its potential towards applications including axial compressive loads. Compression experiments have been conducted on a simply-supported spindle-shaped Tensairity column and displacements have been measured in several positions along the span, whereas axial forces have been experimentally determined by strain gauges measurements. Comparisons has been made between experimental results, finite element and analytical predictions they have already developed, and a good agreement has been found. Moreover, Nguyen et al. (2012) studied an analytical approach to approximate the critical load for an HOWF 3D Timoshenko. Regarding the buckling behavior, the model of proposed inflatable beam proved a prosperity adjustment with the previous models in literature. The total Lagrangian form of Timoshenko kinematics and virtual work principles were applied to formulate the beam's governing equations.

Although there have been many studies focusing on development of numerical methods, the character of orthotropic fabric in influent state has not been handled yet.

3. Motivation of the thesis

Nowadays, there are two approaches existing in literature to analyze the behaviors of the inflatable structures, including the analytical techniques and numerical methods. But most of the previous studies have considered the isotropic fabric materials. The fact is that there is a lack of studing on the orthotropic characters for the woven fabric composite materials.

Therefore, the research motivation of the thesis is to extend an Isogeometric method based on a quadratic NURBS-based Timoshenko beam element with C1-type continuity. This proposed approach is utilized to study the nonlinear buckling behaviour of the orthogonal fibre-laminated fabrics beam.

4. The objectives and scope of the study

The aim of this study is to contribute to the development of an efficient numerical method for analyzing the inflatable structures structures. In this work, orthogonal fibre-laminated fabrics beam is considered as the study object. This thesis will focus on the following problems.

- Applying the "Isogeometric Analysis- IGA" numerical computation to determine the critical load for the composite woven fabric's inflatable beam structure with different boundary conditions. A piece of code in MatLAB was also developed.

- Determine textile composite material constants. These constants are used as input data for calculation programs.

- Determine critical load of steam beam structures of composite textile materials with different boundary conditions.

- Investigate the effect of initial internal pressure on the strength of the inflatable beam.

- Investigate the effect of initial internal pressure on critical load causing buckling of inflatable beam structure.

5. Methodology

In order achieve the study scopes, this thesis have used several methods as follows.

- Studying literature review related to the subjects of textile composite materials and inflatable structures.

- Refer, study and synthesize critical load calculation models for inflatable beam structures of composite textiles to choose a suitable model for analytical equations and finite element calculation models. The goal of this section is to have more analytical tools and traditional finite element tools to verify the IGA calculation results and the experimental results of the thesis.

- Review of NURBS-based geometry and isogeometric analysis (IGA).

- Derive theories for nonlinear buckling analysis of inflatable composite structures under the IGA framework and investigate numerical models.

- Construct analytical model and experiment program for verifying the proposed theory.

6. Outline of the thesis

The contents of this thesis are briefly organized as follows.

- Chapter 1 devotes an introduction to the textile composite materials and structures, focusing on the application of inflatable components. The significances and contributions of the study are pointed out. It could be observed that constructing an effective analysis model for inflatable structures is essential.

- Chapter 2 gives a brief of NURBS (Non-Uniform Rational B-Spline) based geometric description, focusing on 1D problems. Bezier and B-Spline geometries, which are the antecedents of NUBRS, are also recalled. Refinement techniques and the definition of continuity are presented. The motivation and concept of IGA are introduced in here. Refinement strategies including h-technique of knot insertion, p-technique of degree elevation and a unique k-refinement are explaned in detals. Local and adaptive refinements are also reviewed. The advantages and disadvantages of IGA comparation and finite elementingmethod are also shown in this chapter.

- Chapter 3 regards to stability of inflating structure. IGA is expanded to interrogate behavior of nonlinear buckling on inflating composite beams. Therefore, this study is dedicated to linear eigen and nonlinear buckling analysis of inflating beams that made of orthotropic technical textiles when using isogeometric analyis. The analysing method based on modelling 3D Timoshenko beam was built with a homogeneous orthotropic woven fabric (HOWF). The established finite elementing model used a quadratic elements of NURBS-based Timoshenko together with C1-type continuity. The effects of geometric nonlinearities and the inflation pressure on the stability behavior of inflating beam with different boundary conditions are assessed. The beam aspect ratios influenced on the buckling load coefficient are also indicated. The achieved results and experimental results are compared with available ones in literature as well.

- Chapter 4 considers linear finite element inflatable beam (LFEIB) model. In this chapter, LFEIB) model is proposed to describe a geometrically nonlinear behavior of HOWF inflatable beam made of presumed linear elastic material. A nonlinear inflatable beam finite element (NLIBFE) model is introduced. IGA using NURBS basis to construct exact geometry and finite element interpolating functions has received numerous attentions.

A HOWF inflating beam based on IGA used quadratic NURBS-based Timoshenko beam element with C1-type continuity. The element formulation is constructed by using the energy concept that accounts for the change in membrane energy and strain energy in bending, which are related to the stiffness matrix of the beam.

In the linear buckling analysis, a mesh converged test on the critical force beam showed the significant improvement of the proposed numerical model. The model is taken in comparison with a standard finite elementing method. The buckling coefficient results were also in a good agreement with those available in literature. In the nonlinear buckling analysis, the method sucessfully traced the load-deflection response of inflating beams.

Two methods FEM and IGA have been applied to verify the numerical method for the inflatable beam model. A simple beam model was simulated and calculated. The IGA method shows that building numerical models for the problem is relatively more accurate.

In future work, an analytical model and experimental program will be conducted to check the validity of the numerical solutions as an initial step of the manufacturing process that could be the base for the application of inflatable structures in Vietnam.

- Chapter 5 presents materials selection, prototyping plan, besides also checks buckling, the relationship between load and curve by varying pressure, etc. An experimental program for buckling behavior of inflatable beams fabricated from woven fabric composites is presented in this chapter. It begins with as brief review of buckling of thin-walled shell structures, followed by the material test of woven fabric composites. Next, the fabrication procedure of inflatable beams and the buckling testing setup are described in detail. Discusion and remarks on the results obtained are then given.

7. Original contributions of the thesis

In this study, the original contributions of the thesis are covered as follows.

- Investigation of an extension of an IGA-based numerical approach for an application in studying the nonlinear buckling behaviors of inflatable beams made from woven fabric composite materials. In the proposed method with a HOWF, the IGA is examined based on the modelling 3D Timoshenko beam. The finite elementing model is established with C1-type continuity via quadratic NURBS-based Timoshenko elements. Additionlly, the biaxial orthotropic mechanical properties of the materal are determined as the material inputs for finite element model and IGA.

- Experimental investigation on determining the critical buckling load and load-carrying capacity of the inflatable composite fabric beams.

- Study on effects of different air pressures to determine the load-displacement relation of the inflatable beam.

8. Significances of the thesis

Nowadays, common building materials include wood, metal, stone, fabric and materials for application in construction field. The inflatable structures have required great demands to alternative the traditional meterials, including inflated columns,

beams and arches. With the continual improvement in the weaving technique, these construction fabrics are often formed into closed tubes, which are inflated to withstand the self and other loads. The advantage between modern textile materials and conventional materials is that the former can be tailored to particular requirements of certain applications, easy to deploy, having lightweight and low volume storage. Such inflatable structures are often employed in the fields of aerospace, civil engineering, military, marine, agriculture and entertainment. This requires a good knowledge about the behaviour of materials for structural design and optimization.

There are still not many in-depth research results on structures as well as stable bearing capacity of inflatable structures given in Vietnam until present. There is a lack of scientific document on referring to the research and application of this new material in construction. Therefore, the thesis with its importance is given to research, develop, build models, determine the mechanical properties of technical fabrics as well as the calculation theories of inflatable structures, for use in construction.

CHAPTER 1: LITERATURE REVIEW

1.1 Introduction

Besides construction materials such as wood, stone, metal ..., fabric materials today are also widely used in construction works. With continuous improvement in the weaving technique, the construction fabrics are becoming more and more resistant. These construction fabrics are often used to form closed tubes, which are infused with air so that the critical bodies and other loads can be loaded. The bellows are the structural foundations in many constructions around the world: moon-based, site model location, stadium dome, exhibition halls, outdoor temporary structures.

The priority of using new materials for structures over type data transmission systems is light weight, easy deployment and rearrangement, it is possible to shape to special shapes image in some applications and use less storage space. Durable, low production costs and low development costs (without the use of tools) also offer various benefits compared to other structures.

1.2 Fibrous composite materials

The development of new composites and applications of composites has been accelerated. The textile structural composite cited in this study should be considered as typical of modern materials. As a well-known definition, a composite is a material composed of two or more distinct phases. Thus, a composite is heterogeneous. The fibrous composites are materials in which one phase acts as a reinforcement of a second one. The second phase is called the matrix. The challenge is to combine the fibers and the matrix to form the most efficient material for the extended application.

Table 1.1 presents typical average or effective properties for unidirectional composites. The designation of the different composites consists of the name of the fiber followed by the name of the matrix. Unidirectional fibrous composites exhibit different properties in different directions. This is reflected in **Table 1.1** by the labels axial and transverse, which refer to properties in the direction of the fiber (axial) and the properties perpendicular to the fiber (transverse). The properties of a unidirectional composite are also a function of the volume fraction of fibers.

Table 1.1 Typical properties of unidirectional composites

Material	**AS4/ 3501-6**	**T300/ 5208**	**Kevlar /epoxy**	**Boron/ Al**	**SCS-6/ Ti-15-3**	**S-2 glass/ epoxy**
Density, g/cm^3 (lb/in^3)	1.52 (0.055)	1.54 (0.056)	1.38 (0.05)	2.65 (0.096)	3.86 (0.14)	2.00 (0.072)
Axial modulus E_1, GPa (Msi)	148 (21.5)	132 (19.2)	76.8 (11.0)	227 (32.9)	221 (32)	43.5 (6.31)
Transverse modulus E_2, GPa (Msi)	10.50 (1.46)	10.8 (1.56)	5.5 (0.8)	139 (20.2)	145 (21)	11.5 (1.67)
Poisson's ratio ν_{12}	0.30	0.24	0.34	0.24	0.27	0.27
Poisson's ratio ν_{23}	0.59	0.59	0.37	0.36	0.40	0.40

Shear modulus G_{12}, GPa (Msi)	5.61 (0.81)	5.65 (0.82)	2.07 (0.3)	57.6 (8.35)	53.2 (7.78)	3.45 (0.50)
Shear modulus G_{23}, GPa (Msi)	3.17 (0.46)	3.38 (0.49)	1.4 (0.20)	49.1 (7.12)	51.7 (7.50)	4.12 (0.60)
Modulus ratio E_1/E_2	12.6	12.3	14.8	1.6	1.5	4.6
Axial tensile strength χ_τ, Mpa (ksi)	2137 (310)	1513 (219.5)	1380 (200)	1290 (187)	1517 (220)	1724 (250)
Transverse tensile strength Y_τ Mpa (ksi)	53.4 (7.75)	43.4 (6.3)	27.6 (4.0)	117 (17)	317 (46)	41.4 (6.0)
Strength ratio χ_τ/Y_τ	27	35	50	11	4.8	42
Axial CTE α_1, $\mu/^0C$ ($\mu/^0F$)	-0.8 (-0.44)	-0.77 (-0.43)	-4 (-2.2)	5.94 (3.3)	6.15 (3.4)	6.84 (3.8)
Transverse CTE α_2, $\mu/^0C$ ($\mu/^0F$)	29 (16)	25 (13.6)	57 (32)	16.6 (9.2)	7.90 (4.4)	29 (16)
Fiber volume fraction V_f	0.62	0.62	0.55	0.46	0.39	0.60
Ply thickness, mm (in)	0.127 (0.005)	0.127 (0.005)	0.127 (0.005)	0.178 (0.007)	0.229 (0.009)	

The initial development and application of advanced fibrous composites were pursued primarily because of the potential for lighter structures. The first applications in the early 1960s were in aerospace structures, where weight critically affects fuel consumption, performance, and pay load, and in sports equipment, where lighter equipment often leads to improved performance. Today fibrous composites are often the materials of choice of designers for a variety of reasons, including low weight, high stiffness, high strength, electrical conductivity low thermal expension, low or high rate of heat transfer, corrosion resistance, longer fatigue life, optimal design, reduced maintenance, fabrication to net shape, and retention of properties at high operating temperature.

1.3 Inflatable composite structures

Advanced lightweight laminated composite structural elements are increasingly being introduced to new designs of modern aerospace structures for enhancing their structural efficiency and performance. The introduction of new fiber materials, such as glass, carbon or aramid fibers with orthotropic material behavior have motivated a deep study of such elements which are used to build membrane and thin shell structures.

Inflatable structures are membrane components made of elastic/plastic fabric textiles that are inflated by using air pressure to maintain the shape and stiffness of these structures. Advantage of inflatable beams is to be able to absort impact loads, toughness and easy assembly, light weight and require little space for storage. Low manufacturing cost is also an effective factor in industrial application.

1.4 Conclusion

The popularity of inflatable structures is due to the fact that they are very efficient light weight structures. Thus a thorough understanding of the stability

behavior of this type of structures is a must for all those who employ them. Unfortunately, very little relevant references have been found on buckling of inflatable structures made of plain woven composites. Moreover, based on the review on literature, it could be observed that constructing an effective analysis model for inflatable structures is essential.

CHAPTER 2: ISOGEOMETRIC ANALYSIS

2.1 Introduction

An overview of NURBS theory focusing on the mathematical description of free-form curves is reviewed in this chapter. More details on NURBS-based modelling can be found in the books of [14]Piegl, L. and Tiller, W. (1997) and [15]Rogers, D.F. (2001). Non-Uniform Rational B-Spline (NURBS) was developed from Bézier curves and surfaces which were proposed in the late 1960s and early 1970s. NURBS curves can represent precisely a wide range of geometry, especially conic sections. NURBS-based geometry has great advantages in flexibility and precision, and hence nowadays becomes the standard for geometric modelling in computer aided design (CAD).

This chapter starts with a short review of Bézier curves that is the antecedent of B-Spline geometry. B-Spline curves are then explained in details since most of the definitions and properties of B-Splines apply to NURBS. Finally, NURBS as a generalization of B-Splines is presented.

2.2 Comparison between IGA and FEM

2.2.1 Advantages of IGA in comparison with FEM

There are some advantages between IGA and conventional FEM briefly addressed as followings: computing domain, firstly, stays preserving at any level of domain discretization and no matter how coarse it is. In the context of connecting mechanics, this leads to the simplification of connecting detection at the interface of two connecting surfaces, especially in the large deformation circumstance where the relative position of these two surfaces usually changing. Additionally, a sliding joint between surfaces can be reproduced precisely and accurately. This is also beneficial for problems that are sensitive to geometric imperfections, for example, shell buckling analysis, boundary layer phenomena, and fluid dynamics analysis.

Secondly, NURBS based CAD models make the mesh generation step is done automatically without the need for geometry clean-up or feature removal. This can lead to a dramatical reduction in time consumption for meshing and clean-up steps, which account approximately 80% of the total analysis time of a problem [23]Cottrell, J.A., Hughes, T.J.R. and Bazilevs, Y. (2009).

Thirdly, the need to communicate with CAD geometry causes effortless and less time-consuming of mesh refinement. This advantage repulses same basis functions which are utilized for both modeling and analysing processes. It can be steadily indicated that the partition of geometry position and the mesh refinement of the computating domain are simplified to knot insertion algorithm, which is performed automatically. These partitioning segments then become new elements and the mesh is exact entirely.

Finally, inter-element regularity higher with the maximum of C^{p-1} in the absence of repeated knots makes the naturally suitable method for mechanics problems. The higher-order element derivatives in formulations as Kirchhoff-Love shell, gradient elasticity, Cahn-Hilliard equation of phasing separation… This results from directly utilizating of B-spline/NURBS are based on analysing calculation. In contrast with FEM's basis functions, which are defined locally in the element's interior with C^0 continuity across element boundaries (and thus the numerical approximation is C^0), IGA's basis functions are not located in one element (knot span). Insteadly, they are usually defined over several contiguous elements which guarantee a greater regularity and interconnectivity. Therefore, the approximation is highly continuous. Furthermore, one another benefit of this higher smoothness is the greater convergence rate in comparison with conventional methods, especially combination of a new type of refinement technique which called *k*-refinement. Nevertheless, it is worthy to mention that the larger support of basis does not lead to bandwidth increment in the numerical approximation and thus the bandwidth of resulted sparse matrix will be retained in the classical FEM's functions.

2.2.2 Disadvantages of IGA

This methodology, however, presents some challenges that require special treatments.

The most significant challenge of making use of B-splines/NURBS in IGA is that its tensor producing structure does not permit a true local refinement. Any knot insertion will lead to global propagation across computational domain.

Due to the lack of Kronecker delta property, in addition, the application of in-homogeneous Dirichlet boundary condition or forces/physical data exchange in a coupled analysis are highly involved.

Furthermore, owing to the larger support of the IGA's basis functions, the resulted system of matrix are relatively denser (containing more non-zero entries) when it compares to the FEM and tri-diagonal banding structure as well.

2.3 B-Spline

Similar to Bézier curves, B-Spline curves are defined by a linear combination of controling points with basis B-Splines functions over a parametric space. The parametric space is divided into interval parts and the B-Splines are defined piecewise on these intervals with certain continuity requirements between the intervals. Since the number of intervals is arbitrary, the polynomial degree can be chosen independently out of the number of control points. Therefore, a large set of data points can be approximated by using low polynomial degree. The parametric space is defined by the so-called knot vector.

2.3.1 Knot Vector

The knot vector is a set of non-decreasing real numbers representing coordinates in parametric space:

$$\Xi = \left\{ \xi_1, \xi_2, \xi_3, ..., \xi_{n+p+1} \right\} \qquad 2.1$$

where $\xi_i \in \mathbb{R}$ is the i^{th} knot, i is the knot index, $i = 1, 2, ..., \mathrm{n+p+1}$, p is the polynomial degree and *n* is the number of basis functions. The intervals $\left[\xi_1, \xi_{n+p+1} \right]$

and $[\xi_i, \xi_{i+1}]$ are called a *patch* and a *knot span*, respectively. A B-Spline basis function is C^{∞} continuous inside a knot span, and C^{p-1} continuous at a single knot. A knot value can be repeated more than once and is then called a multiple knot. If all knots are equally spaced in the parametric space, the knot vector is called *uniform, and non-uniform vice versa.* A knot vector is said to be *open* if the first and the last knot have the multiplicity $p+1$. In a B-Spline with an open knot vector, the first and the last control points are interpolated and the curve is tangential to the control polygon at the start and the end of the curve.

2.3.2 B-Spline Basis Functions

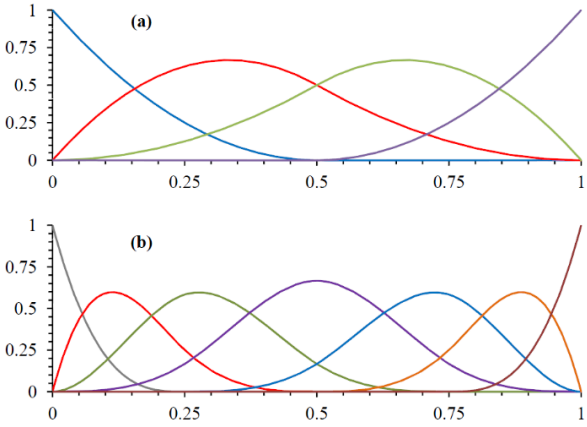

Figure 2.1 (a) Quadratic B-spline basis functions for an open, non-uniform knot vector $\Xi = \{0,0,0,0.5,1,1,1\}$. (b) Cubic B-spline basis functions for an open, non-uniform knot vector $\Xi = \{0,0,0,0,0.25,0.5,0.75,1,1,1,1\}$

B-Splines basis functions $N_{i,p}(\xi)$ of degree $p \geq 0$ are defined by the Cox-deBoor recursive formula [10]Thai, C. H., Ferreira, A. J. M., Carrera, E., & Nguyen-Xuan, H. (2013) and [11]Benson, D. J., Bazilevs, Y., Hsu, M. C., & Hughes, T. J. R. (2011), as follows:

$$N_{i,0}(\xi) = \begin{cases} 1 & if\ \xi_i \leq \xi_{i+1} \\ 0 & otherwise, \end{cases} \qquad 2.2$$

$$N_{i,p}(\xi) = \frac{\xi - \xi_i}{\xi_{i+p} - \xi_i} N_{i,p-1}(\xi) + \frac{\xi_{i+p+1} - \xi}{\xi_{i+p+1} - \xi_{i+1}} N_{i+1,p-1}(\xi) \qquad 2.3$$

Important properties of B-Spline basis functions are:

Partition of unity, i.e. $\sum_{i=1}^{n} N_{i,p}(\xi) = 1$

- Non-negativity, i.e. $N_{i,p}(\xi) \geq 0$
- Local support, i.e. $N_{i,p}(\xi)$ is non-zero only in the interval $[\xi_i, \xi_{i+p+1}]$
- Linear independence, i.e. $\sum_{i=1}^{n} \alpha_i N_i^p(\xi) = 0 \Leftrightarrow \alpha_{i,j} = 0$

Examples of quadratic and cubic B-Spline basis functions for open, non-uniform knot vectors are presented in

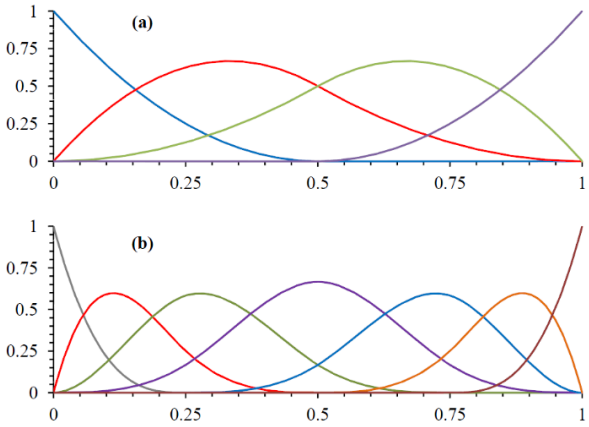

Figure 2.1. The derivatives of the B-Spline basis functions are computed by the following formula [5]Wolfgang A. Wall, Moritz A. Frenzel, Christian Cyron. (2008):

$$N_{i,p}^{(k)} = \frac{p}{p-k}\left(\frac{\xi-\xi_i}{\xi_{i+p}-\xi_i}N_{i,p-1}^{(k)} + \frac{\xi_{i+p+1}-\xi}{\xi_{i+p+1}-\xi_{i+1}}N_{i+1,p-1}^{(k)}\right) with \qquad k=0,\ldots,p-1 \qquad 2.4$$

2.3.3 B-Spline Curves

A B-Spline curve of p order is defined by a tensor product of B-spline basis functions and control points, as follows:

$$C(\xi) = \sum_{i=1}^{n} N_{i,p}(\xi) P_i \qquad 2.5$$

Control points $P_i \in \mathbb{R}^d, i = 1,2,\ldots,n$ are points in d-dimensional physical space $\mathbb{R}^d$, and construct the *control polygon.* In **Figure 2.2** a quadratic B-Spline curve with open knot vector is given. As can be seen, the first and last control point are interpolated and the curve is tangential to the control polygon at its start and end. The derivative of a B-Spline curve is also a B-spline curve which is computed by the following formula [3]T.J.R. Hughes, J.A. Cottrell, Y. Bazilevs. (2005):

$$C^{(k)}(\xi) = \sum_{i=0}^{n-k} N_{i,p-k}(\xi) P_i^{(k)} \qquad 2.6$$

$$P_i^{(k)} = \begin{cases} P_i & k=0 \\ \dfrac{p-k+1}{u_{i+p+1}-u_{i+k}}\left(P_{i+1}^{(k-1)} - P_i^{(k-1)}\right) & k>0 \end{cases} \qquad 2.7$$

Some important characteritics of B-spline curves are:

- Convex hull property: the inside curve contained in the convex hull of controling polygon.
- The controling points are generally not interpolated.

- The controling points influences on maximum sections.
- For open knot vectors, the first and last controling point are interpolated. The curve is tangential to the controling polygon at the beginning and the end of the curve. The continuous curve between two knots and continuous at one knot having multiplicity k.
- Affine transforming of the B-Spline curve are performed correspondingly by transforming the controling points.
- A Bézier curve is also a B-Spline curve but with only one interval knot.

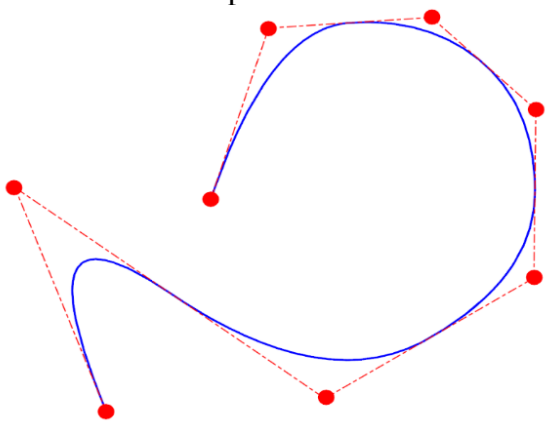

Figure 2.2 B-Spline, piecewise quadratic curve in $\mathbb{R}^2$ and corresponding control polygon

2.4 NURBS Curves

As mentioned on above content, NURBS is abbreviation for Non-Uniform Rational B-Splines. In term of non-uniform, it refers to knot vector which is generally unchanged. Other term named rational term shall refer to the basis functions. For B-Splines, the basis functions are known as incoherent polynomials. For NURBS they are piecewise rational polynomials. A rational B-Spline curve in $\mathbb{R}^d$ is the projection onto d-dimensional physical space of a non-rational (polynomial) B-spline curve defined in $d+1$-dimensional homogeneous coordinate space. In three-dimensional Euclidean space, the control points $R_{i,p}(\xi) = \dfrac{N_{i,p}(\xi) w_i}{\sum_{i=1}^{n} N_{i,p}(\xi) w_i}$.

Then homogeneous four-dimensional control points are written as [6]Kiendl, J., Bletzinger, K. U., Linhard, J., & Wüchner, R. (2009):

$$P^w = (wx, wy, wz, w) = (X, Y, Z, W), w \neq 0, \quad 2.8$$

and the non-rational B-Spline curve is obtained as follows:

$$C^w(\xi) = \sum_{i=1}^{n} N_{i,p}(\xi) P_i^w \quad 2.9$$

Projecting back into three-dimensional space by using a mapping, denoted by [6]Kiendl, J., Bletzinger, K. U., Linhard, J., & Wüchner, R. (2009).

$$P = H\{P^w\} = H\{(X, Y, Z, W)\} = \begin{cases} (X/W, Y/W, X/W) \; if \; W \neq 0 \\ direction(X, Y, Z) \quad if \; W = 0 \end{cases} \quad 2.10$$

the rational B-Spline curve is yielded as:

$$C(\xi) = \left(x(\xi), y(\xi), z(\xi)\right) = \frac{\sum_{i=1}^{n} N_{i,p}(\xi) w_i P_i}{\sum_{i=1}^{n} N_{i,p}(\xi) w_i} \quad 2.11$$

Defining NURBS basis functions as:

$$R_{i,p}(\xi) = \frac{N_{i,p}(\xi) w_i}{\sum_{i=1}^{n} N_{i,p}(\xi) w_i} \quad 2.12$$

one can write a NURBS curve in the common way as the sum of control points times the respective basis functions:

$$C(\xi) = \sum_{i=1}^{n} R_{i,p}(\xi) P_i \quad 2.13$$

If all controling weights are equilibrium, the rational formula in **Eq. 2.122** scale down to the normal B-Spline functions. It means that this B-Spline is a particular case of NURBS with equilibrium controling weights, and all properties of B-Splines listed in **Section 2.3.3** apply to NURBS as well. The significant superiority of the basis rational functions is that they allow an exact shape of conic sections. The sections include circle and ellipse curves.

2.5 Isogeometric Analysis

The idea of isogeometric analysis is that the functions used for the geometry description in CAD are adopted by the analysis for the geometry and the solution field. By this, the whole process of meshing can be omitted and the two models for design and analysis merge into one. The schematic illustration of NURBS paraphernalia is illustrated in **Figure 2.3**

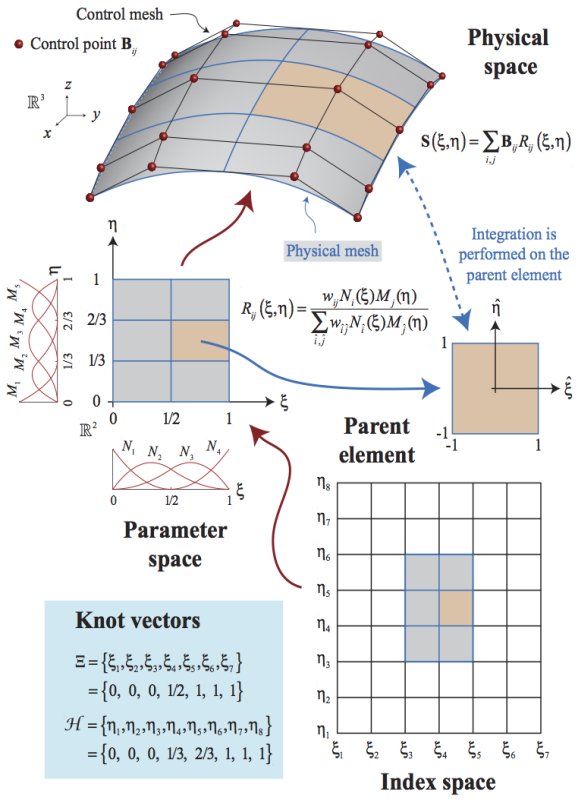

Figure 2.3 Schematic illustration of NURBS paraphernalia for a one-patch surface model. (Source: [19]Hughes, T.J.R., Cottrell, J.A. and Bazilevs, Y. (2005))

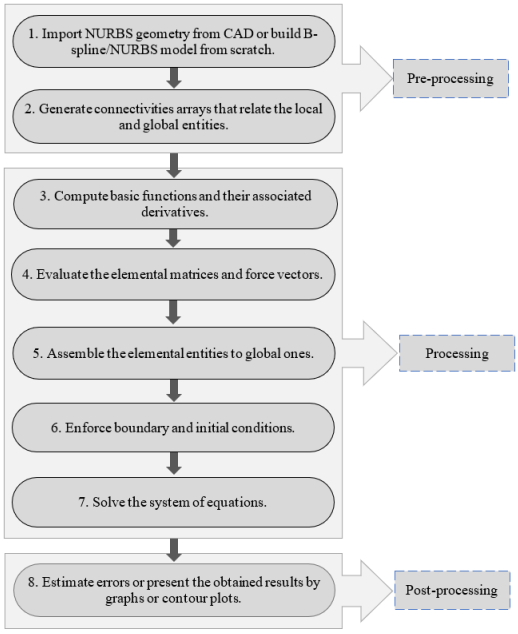

Figure 2.4 Summary of IGA procedure

2.6 Isogeometric NURBS-elements

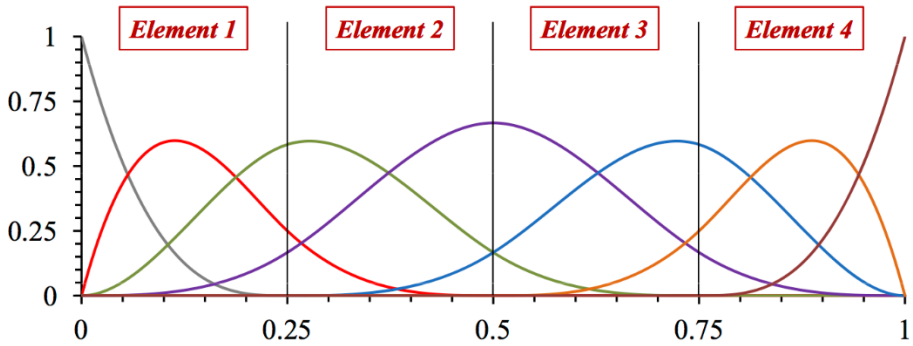

Figure 2.5 Isogeometric NURBS-elements

A NURBS patch is defined over a parametric domain, which is divided into intervals by non-zero knot spans. These intervals are defined as elements. An example of NURBS elements is illustrated **Figure 2.4**. The reason for this definition is that inside a knot interval, B-Spline basis functions are polynomials and therefore Gauss quadrature can be used for integration on element level.

The following important properties of NURBS as basis for analysis are summarized:

- The basis functions fulfill the requirements of linear independence and partition of unity. They have a local support, depending on the polynomial degree.

- Basis functions have higher-order continuities over element boundaries.
- Degrees of freedom are defined on the control points.
- The isoparametric concept is used.
- Rigid body motions are treated correctly (zero strains) due to the affine covariance property of NURBS.
- Locking effects stemming from low-order basis functions can be precluded efficiently.

2.7 Isogeometric Analysis versus Classical Finite Element Analysis

Major differences are listed in **Table 2.1**. On the other hand, isogeometric analysis and classical finite element share many common features. For instance, they are both isoparametric implementations of Galerkins method, accordingly, isogeometric analysis inherites the computing implementation of finite element procedure. Others are given in **Table 2.2**.

Table 2.1 NURBS based isogeometric analysis versus classical finite element analysis. (Source: [5]Wolfgang A. Wall, Moritz A. Frenzel, Christian Cyron. (2008))

Isogeometric analysis	**Classical finite element analysis**
- Exact geometry	- Approximate geometry
- Control points	- Nodal points
- Control variables	- Nodal variables
- Basis does not interpolate control points and variables	- Basis interpolates nodal points and variables
- NURBS basis	- Polynomial basis
- High, easily controlled continuity	- C^0-continuity, always fixed
- *hpk*-refinement space	- *hp*-refinement space
- Pointwise positive basis	- Basis not necessarily positive
- Convex hull property	- No convex hull property
- Variation diminishing in the presence of discontinuous data	- Oscillatory in the presence of discontinuous data

Table 2.2 Common features shared by isogeometric analysis and classical finite element analysis. (Source: [5]Wolfgang A. Wall, Moritz A. Frenzel, Christian Cyron. (2008))

Isoparametric concept
Galerkins method
Code architecture
Compactly supported basis
Bandwidth of matrices
Partition of unity
Affine covariance
Patch tests are satisfied

2.8 Conclusion

- The fundamental developments of Isogeometric Analysis in this chapter are summarized as follows:

- A concept explaining the ultimate goal of eliminating the conversion from CAD files to CAE codes is IGA. It is accomplished by employing the same basis functions of CAD for analysing.

- B-spline basis functions from the so-called knot vector can readily be computed by the Cox-de Boor algorithm. Its associating derivatives can be expressed as linear combination of the lower order bases.

- B-spline curve is defined by a linear combination of basis functions and corresponding control points. B-spline surface and volume are defined analogously by taking advantage of tensor product structure of B-splines.

- B-splines offers three kinds of mesh refinement which are named h-refinement, p-refinement and k-refinement. While the first two techniques are fairly equivalent to element subdivision and order rising in FEA, respectively, the third one is exclusive to B-splines which results in higher interelement continuity.

- NURBS in d is defined by conic projecting B-splines in d+1, where the coordinates of the (d+1)th dimension are the strictly positive weights. This transformation has the ability to represent exact conic sections.

- NURBS geometry therefore is defined similarly as B-spline one.

- Numerical integration in NURBS-based IGA is performed via two successive mappings, the first one is from natural/parent space to parametric space and the second one is from parametric space to physical space.

- Since the same B-spline/NURBS curve can be represented by concatenated.

- Bézier curves, one can decompose the B-spline/NURBS curve into several C0 Bézier elements for using in the analysis. This procedure makes the IGA approach backward compatible with conventional FEM codes.

CHAPTER 3: ANALYTICAL THEORY OF INFLATABLE COMPOSITE BEAMS

3.1 Introduction

A large number of analytical analyses related to the inflating beams and arches are available in literature, concerning both theoretical and experimental analysis. One important aspect is need to build the best adapted analytical modeling for beam structures. Euler-Bernoulli kinematics and the Timoshenko kinematics are widely used to gain the analytical solutions and to develop the formulations for inflating beams made of woven fabrics.

The finite element model established here uses a quadratic NURBS-based Timoshenko elements with C^1-type continuity. The effects of geometric nonlinearities and the inflation pressure on the stability behavior of inflatable beam with different boundary conditions are assessed. The influence of the beam aspect ratios on the buckling load coefficient are also pointed out. The obtained results are also compared with ones available in literature as well as experimental results.

3.2 Inflatable beam models.

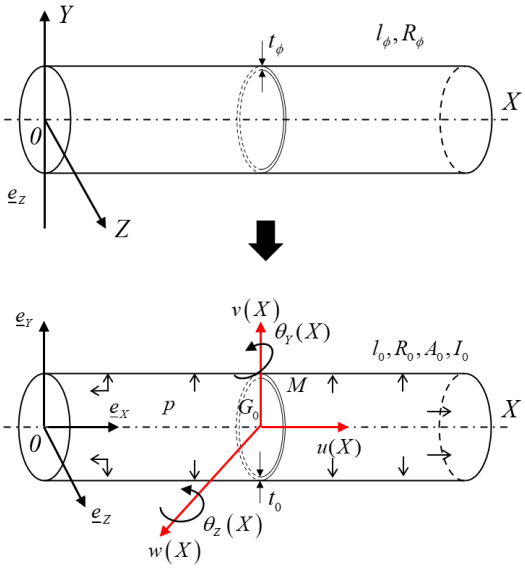

Figure 3.1 HOWF inflatable beam: (a) in natural state and (b) in the reference configuration (inflated state)

Figure 3.1 shows an inflatable cylindrical beam made of an HOWF. l_0, R_0, t_0, A_0 and I_0

$$A_0 = 2\pi R_0 t_0 \tag{3.1}$$

$$I_0 = \frac{A_0 R_0^2}{2} \tag{3.2}$$

$$l_0 = l_\phi + \frac{pR_\phi l_\phi}{2E_t t_\phi}\left(1 - 2\nu_{lt}\right) \tag{3.3}$$

$$R_0 = R_\phi + \frac{pR_\phi^2}{2E_t t_\phi}\left(2 - \nu_{lt}\right) \tag{3.4}$$

$$t_0 = t_\phi + \frac{3pR_\phi}{2E_t}\nu_{lt} \tag{3.5}$$

in which l_ϕ, R_ϕ and t_ϕ are respectively the length, the fabric thickness, and the external radius of the beam in the natural state.

The internal pressure p is assumed to remain constant,

The slenderness ratio is $\lambda_s = \frac{L}{\rho}$ where $L = \mu l_0$ is the beam length and $\rho = \sqrt{\frac{I_0}{A_0}}$ is the beam radius of gyration. The coefficient μ takes different values according to the boundary conditions of the beam.

M is a point on the current cross-section and G_0 the centroid of the current cross-section lies on the X - *axis*. The beam is undergoing axial loading. Two Fichter's simplifying assumptions are applied in the following:

- The cross-section of the inflated beam under consideration is assumed to be circular and maintains its shape after deformation, so that there are no distortion and local buckling;
- The rotations around the principal inertia axes of the beam are small and the rotation around the beam axis is negligible.

3.3 Theoretical formulation

3.3.1 Kinematics

With the hypotheses proposed by Fichter were applied, the displacement components of an arbitrary point *M(X, Y, Z)* on the beam are:

$$\underline{\mathbf{u}}(M)=\begin{Bmatrix}\underline{u}_X\\ \underline{u}_Y\\ \underline{u}_Z\end{Bmatrix}=\begin{Bmatrix}u(X)\\ v(X)\\ w(X)\end{Bmatrix}+\begin{Bmatrix}Z\theta_Y(X)\\ 0\\ 0\end{Bmatrix}+\begin{Bmatrix}-Y\theta_Z(X)\\ 0\\ 0\end{Bmatrix} \qquad 3.6$$

Where $\underline{u}_X, \underline{u}_Y$ and $\underline{u}_Z$ are the components of the displacement at the arbitrary point *M*, whilst $u(X), v(X)$ and $w(X)$ correspond to the displacements of the centroid G_0 of the current cross-section at abscissa X, related to the base (X, *Y, Z*); $\theta_Y(X)$ and $\theta_Z(X)$ are the rotations of the current section at abscissa X around both principal axes of inertia of the beam, respectively. Let $\delta\underline{\mathbf{u}}$ denote an arbitrary virtual displacement from the current position of the material point M:

$$\delta\underline{\mathbf{u}}=\begin{Bmatrix}\delta u(X)\\ \delta v(X)\\ \delta w(X)\end{Bmatrix}+\begin{Bmatrix}Z\delta\theta_Y(X)\\ 0\\ 0\end{Bmatrix}+\begin{Bmatrix}-Y\delta\theta_Z(X)\\ 0\\ 0\end{Bmatrix} \qquad 3.7$$

The definition of the strain at an arbitrary point as a function of the displacements is:

$$\underline{\underline{\mathbf{E}}}=\underline{\underline{\mathbf{E}}}_l+\underline{\underline{\mathbf{E}}}_{nl} \qquad 3.8$$

Where $\mathbf{E}_t$ and $\mathbf{E}_{nl}$ are the Green-Lagrange linear and nonlinear strains, respectively. The nonlinear term $\mathbf{E}_{nl}$ takes into account the geometrical nonlinearities. The strain fields depend on the displacement fields as following:

$$\underline{\underline{\mathbf{E}}}_l = \begin{Bmatrix} \dfrac{\partial u_X}{\partial X} \\ \dfrac{\partial u_Y}{\partial Y} \\ \dfrac{\partial u_Z}{\partial Z} \\ \dfrac{\partial u_X}{\partial Y} + \dfrac{\partial u_Y}{\partial X} \\ \dfrac{\partial u_X}{\partial Z} + \dfrac{\partial u_Z}{\partial X} \\ \dfrac{\partial u_Y}{\partial Z} + \dfrac{\partial u_Z}{\partial Y} \end{Bmatrix}, \underline{\underline{\mathbf{E}}}_{nl} = \begin{Bmatrix} \dfrac{1}{2}\underline{\mathbf{u}}_{,X}^T \underline{\mathbf{u}}_{,X} \\ \dfrac{1}{2}\underline{\mathbf{u}}_{,Y}^T \underline{\mathbf{u}}_{,Y} \\ \dfrac{1}{2}\underline{\mathbf{u}}_{,Z}^T \underline{\mathbf{u}}_{,Z} \\ \dfrac{1}{2}\underline{\mathbf{u}}_{,X}^T \underline{\mathbf{u}}_{,Y} + \dfrac{1}{2}\underline{\mathbf{u}}_{,Y}^T \underline{\mathbf{u}}_{,X} \\ \dfrac{1}{2}\underline{\mathbf{u}}_{,X}^T \underline{\mathbf{u}}_{,Z} + \dfrac{1}{2}\underline{\mathbf{u}}_{,Z}^T \underline{\mathbf{u}}_{,X} \\ \dfrac{1}{2}\underline{\mathbf{u}}_{,Y}^T \underline{\mathbf{u}}_{,Z} + \dfrac{1}{2}\underline{\mathbf{u}}_{,Z}^T \underline{\mathbf{u}}_{,Y} \end{Bmatrix} \quad 3.9$$

The higher-order nonlinear terms are the product of the vectors that are defined as

$$\underline{\mathbf{u}}_{,X} = \begin{Bmatrix} u_{X,X} \\ u_{Y,X} \\ u_{Z,X} \end{Bmatrix}, \underline{\mathbf{u}}_{,Y} = \begin{Bmatrix} u_{X,Y} \\ u_{Y,Y} \\ u_{Z,Y} \end{Bmatrix}, \underline{\mathbf{u}}_{,Z} = \begin{Bmatrix} u_{X,Z} \\ u_{Y,Z} \\ u_{Z,Z} \end{Bmatrix} \quad 3.10$$

3.3.2 Constitutive equations

The Saint Venant-Kirchhoff orthotropic material is used in recent work. The energy function $\Phi_E = \Phi\left(\underline{\underline{\mathbf{E}}}\right)$ related to this case is known as the Helmholtz free-energy function.

To describe the behavior of the inflatable beam, we define two coordinate systems: A local warp and weft direction coordinate system related to each point of the membrane coincident with the principal directions of the fabric **Figure 3.2a**. And the other is the Cartesian coordinate system attached to the beam **Figure 3.2b**.

The components of the second Piola-Kirchhoff tensor $\underline{\underline{S}}$ are given by the nonlinear Hookean stress-strain relationships

$$\underline{\underline{\mathbf{S}}} = \underline{\underline{\mathbf{S}}}^o + \frac{\partial \Phi}{\partial \underline{\underline{\mathbf{E}}}} = \underline{\underline{\mathbf{S}}}^o + \underline{\underline{\mathbf{C}}}.\underline{\underline{\mathbf{E}}} \quad 3.11$$

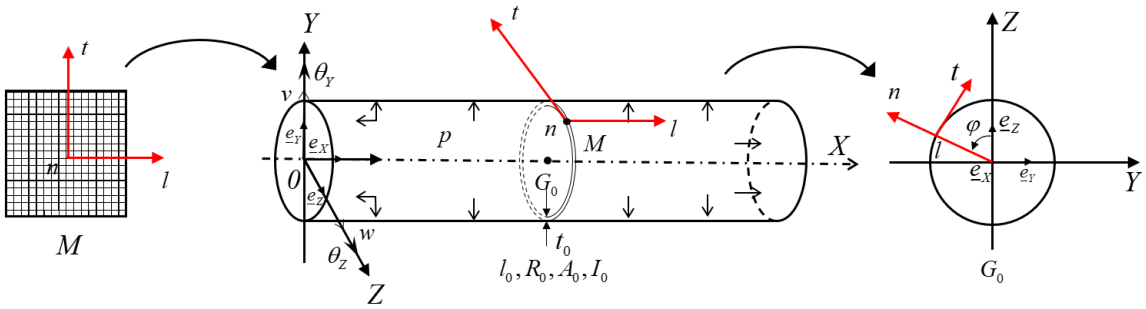

Figure 3.2 (a) Fabric local coordinate system, (b) Beam Cartesian coordinate system

where

- $\underline{\underline{\mathbf{S}}}^{o}$ is the inflation pressure prestressing tensor.
- the second Piola-Kirchhoff tensor is written in the beam coordinate system as

$$\underline{\underline{\mathbf{S}}} = \begin{bmatrix} S_{XX} & S_{XY} & S_{XZ} \\ & S_{YY} & S_{YZ} \\ symmetrical & & S_{ZZ} \end{bmatrix} \tag{3.12}$$

- $\underline{\underline{\underline{\underline{\mathbf{C}}}}}$ is the fourth-order elasticity tensor expressed in the beam axes.

In general, the inflation pressure prestressing tensor is assumed spheric and isotropic [50]Wielgosz, C. (2005) . So,

$$\underline{\underline{\mathbf{S}}}^{o} = S^{o}\underline{\underline{\mathbf{I}}} \tag{3.13}$$

Where $\underline{\underline{\mathbf{I}}}$ is the identity second order tensor and $S^{o} = \frac{N_o}{A_o}$ is the prestressing scalar. The elasticity tensor expressed in the beam axes can be calculated from the local orthotropic elasticity tensor using the rotation matrix *R* (see [54]Apedo, K. L., Ronel, S., Jacquelin, E., Massenzio, M., & Bennani, A. (2009)):

$$C_{ijkl} = R_{im}R_{jn}R_{kp}R_{lq}C^{loc}_{mnpq} \tag{3.14}$$

With *i, j, k, m, n, p, q* = 1, …, 3, where

$$\underline{\underline{\underline{\mathbf{R}}}} = \begin{bmatrix} 1 & 0 & 0 \\ 0 & \cos\varphi & -\sin\varphi \\ 0 & \sin\varphi & \cos\varphi \end{bmatrix} \tag{3.15}$$

and

$$\underline{\underline{\underline{\underline{\mathbf{C}}}}}^{loc} = \begin{bmatrix} C_{11} & C_{12} & 0 \\ C_{12} & C_{22} & 0 \\ 0 & 0 & C_{66} \end{bmatrix} \tag{3.16}$$

The elasticity tensor in the beam axes then obtained as

$$\underline{\underline{\underline{\underline{\mathbf{C}}}}} = \begin{bmatrix} C_{11} & c^2C_{12} & s^2C_{12} & csC_{12} & 0 & 0 \\ & c^4C_{22} & c^2s^2C_{22} & c^3sC_{22} & 0 & 0 \\ & & s^4C_{22} & cs^3C_{22} & 0 & 0 \\ & & & c^2s^2C_{22} & 0 & 0 \\ & & & & s^2C_{66} & csC_{66} \\ symmetrical & & & & & c^2C_{66} \end{bmatrix} \tag{3.17}$$

Where $c = \cos\varphi$ and $s = \sin\varphi$ with $\varphi = (e_Z, n)$

the angle between the *Z*-axis of the beam and the normal of the membrane at the current point. The tensor components are described as a function of the mechanical properties of the HOW fabric:

$$C_{11}=\frac{E_t}{1-\nu_{lt}\nu_{tl}};C_{12}=\frac{E_l\nu_{tl}}{1-\nu_{lt}\nu_{tl}};$$

$$C_{22}=\frac{E_t}{1-\nu_{lt}\nu_{tl}};C_{66}=G_{lt}\qquad and\quad \frac{E_l}{\nu_{lt}}=\frac{E_t}{\nu_{tl}}$$

3.3.3 Virtual work principle

The balance equations of an inflatable beam come from the virtual work principle (VWP). The VWP applied to the beam in its pressurized state is

$$\delta W_{\text{int}}=\delta W_{ext}^{d}+\delta W_{ext}^{p},\forall\delta\underline{\mathbf{u}} \tag{3.18}$$

$$\Leftrightarrow\int_{V_o}\underline{\underline{\mathbf{S}}}:\delta\underline{\underline{\mathbf{E}}}dV_o=\int_{V_o}\mathrm{f}.\delta\underline{\mathbf{u}}dV_o+\left\{R.\delta\underline{\mathbf{u}}\right\}+\int_{\partial V_o}\mathrm{t}.\delta\underline{\mathbf{u}}dA,\forall\delta\underline{\mathbf{u}} \tag{3.19}$$

where f and t are the body forces per unit volume and the traction forces per unit area, respectively; R represents the reactions. The internal virtual work δW_{int} on the left-hand-side of **Eq. 3.18** is formulated from the second Piola-Kirchhoff tensor $\mathbf{S}$ and the virtual Green strain $\delta\underline{\underline{\mathbf{E}}}$.

The virtual Green strain tensor is written in the beam coordinate system as

$$\delta\underline{\underline{\mathbf{E}}}=\delta\underline{\underline{\mathbf{E}}}_l+\delta\underline{\underline{\mathbf{E}}}_{nl} \tag{3.20}$$

Where

$$\delta\underline{\underline{\mathbf{E}}}_l=\begin{bmatrix}\delta E_{XX}^{l} & \delta E_{YY}^{l} & \delta E_{ZZ}^{l} & \delta E_{YZ}^{l} & \delta E_{ZX}^{l} & \delta E_{XY}^{l}\end{bmatrix}^T \tag{3.21}$$

$$\delta\underline{\underline{\mathbf{E}}}_{nl}=\begin{bmatrix}\delta E_{XX}^{nl} & \delta E_{YY}^{nl} & \delta E_{ZZ}^{nl} & \delta E_{YZ}^{nl} & \delta E_{ZX}^{nl} & \delta E_{XY}^{nl}\end{bmatrix}^T \tag{3.22}$$

With

$$\begin{aligned}
\delta E_{XX}^{l}&=\delta u_{,X}+Z\delta\theta_{Y,X}-Y\delta\theta_{Z,X}\\
\delta E_{YY}^{l}&=0\\
\delta E_{ZZ}^{l}&=0\\
\delta E_{YZ}^{l}&=0\\
\delta E_{XZ}^{l}&=\delta w_{,X}+\delta\theta_{Y,X}\\
\delta E_{XY}^{l}&=\delta v_{,X}-\delta\theta_{Z}
\end{aligned} \tag{3.23}$$

and

$$\begin{aligned}
\delta E_{XX}^{nl}=&\left(u_{,X}+Z\theta_{Y,X}-Y\theta_{Z,X}\right)\delta u_{,X}+v_{,X}\delta v_{,X}\\
&+w_{,X}\delta w_{,X}+Z\left(u_{,X}+Z\theta_{Y,X}-Y\theta_{Z,X}\right)\delta\theta_{Y,X}\\
&-Y\left(u_{,X}+Z\theta_{Y,X}-Y\theta_{Z,X}\right)\delta\theta_{Z,X}
\end{aligned}$$

$$
\begin{aligned}
\delta E_{YY}^{nl} &= \theta_Z \delta\theta_Z \\
\delta E_{ZZ}^{nl} &= \theta_Y \delta\theta_Y \\
\delta E_{YZ}^{nl} &= \left(\theta_Z \delta\theta_Y + \theta_Y \delta\theta_Z\right) \\
\delta E_{XZ}^{nl} &= \theta_Y \delta u_{,X} + \left(u_{,X} + Z\theta_{Y,X} - Y\theta_{Z,X}\right)\delta\theta_Y \\
&\quad + Z\theta_Y \delta\theta_{Y,X} - Y\theta_Y \delta\theta_{Z,X} \\
\delta E_{XY}^{nl} &= -\theta_Z \delta u_{,X} - Z\theta_Z \delta\theta_{Y,X} \\
&\quad - s\left(u_{,X} + Z\theta_{Y,X} - Y\theta_{Z,X}\right)\delta\theta_Z + Y\theta_Z \delta\theta_{Z,X}
\end{aligned}
\qquad 3.24
$$

The generalized resultant forces and moments, and the quantities $Q_i\,(i=1,...,10)$ acting over the reference cross-section A_o can be related to the stresses in the beam by

$$
\begin{Bmatrix} N \\ T_y \\ T_z \\ M_y \\ M_z \end{Bmatrix} = \int_{A_o} \begin{Bmatrix} S_{XX} \\ S_{XY} \\ S_{XZ} \\ ZS_{XX} \\ -YS_{XX} \end{Bmatrix} dA_o \qquad 3.25
$$

$$
Q_i = \int_{A_o} \begin{Bmatrix} -YZS_{XX} \\ Z^2 S_{XX} \\ -ZS_{XY} \\ ZS_{XZ} \\ Y^2 S_{XX} \\ YS_{XY} \\ -YS_{XZ} \\ S_{YY} \\ S_{ZZ} \\ -S_{YZ} \end{Bmatrix} dA_o, \qquad i = 1,...,10 \qquad 3.26
$$

where, N corresponds to the axial force, T_y and T_z to the shear force in Y and Z directions respectively, M_y and M_z to the bending moments about the Y and Z-axis. Quantities Q_i depend on the initial geometry of the cross-section.

Then the internal virtual work may be written as:

$$-\delta W_{\text{int}} = \int_0^{l_o} \begin{Bmatrix} A_1(X) \\ B_1(X) \\ C_1(X) \\ D_1(X) \\ E_1(X) \\ F_1(X) \\ H_1(X) \end{Bmatrix}^T \times \begin{Bmatrix} \delta u_{,X} \\ \delta v_{,X} \\ \delta w_{,X} \\ \delta\theta_{,X} \\ \delta\theta_{Y,X} \\ \delta\theta_Z \\ \delta\theta_{Z,X} \end{Bmatrix} dX \qquad 3.27$$

The external virtual work δW_{ext} is due to the dead loads and to the pressure load.

The dead loads, which may include concentrated loads and moments as well as distributed loads, act like the body forces. The inflation pressure plays a role of a traction force acting on the cylindrical surface and on both ends. The first term on the right side of **Eq. 3.19** can be rewritten as

$$\delta W_{ext}^d = \int_0^{l_o} \begin{Bmatrix} f_x \\ f_y \\ f_z \end{Bmatrix} \times \begin{Bmatrix} \delta u \\ \delta v \\ \delta w \end{Bmatrix} dX + \sum_{i=1}^{n} \begin{Bmatrix} F_X(X_i) \\ F_Y(X_i) \\ F_Z(X_i) \\ M_Y(X_i) \\ M_Z(X_i) \end{Bmatrix} \times \begin{Bmatrix} \delta u(X_i) \\ \delta v(X_i) \\ \delta w(X_i) \\ \delta\theta_Y(X_i) \\ \delta\theta_Z(X_i) \end{Bmatrix} \qquad 3.28$$

In which f_x, f_y and f_z are respectively the distributed loads along the X, *Y*, and *Z* axes, while $F_a(b)$, and $M_a(b)$ (With $a = X, Y, Z; b = X_1, ..., X_n$) are the external support reactions and the external loads and moments.

The second term on the right side of **Eq. 3.19** is the external virtual work due to the inflation pressure. This virtual work includes the pressure virtual work on the cylindrical surface δW_{cyl}^p and on both ends δW_{end}^p, **Figure 3.3** shows a reference cylindrical inflated beam with an applied uniform pressure *p* acting on the cylindrical surface *A* which has a pointwise normal $\underline{\mathbf{n}}$ in the current configuration. The traction force vector **t** in **Eq. 3.19** is therefore $p\underline{\mathbf{n}}$ and the virtual work due to the inflation pressure δW_{ext}^p is then given by

$$\delta W_{ext}^p = \delta W_{cyl}^p + \delta W_{end}^p = \int_A p\underline{\mathbf{n}}.\delta\underline{\mathbf{u}} dA \qquad 3.29$$

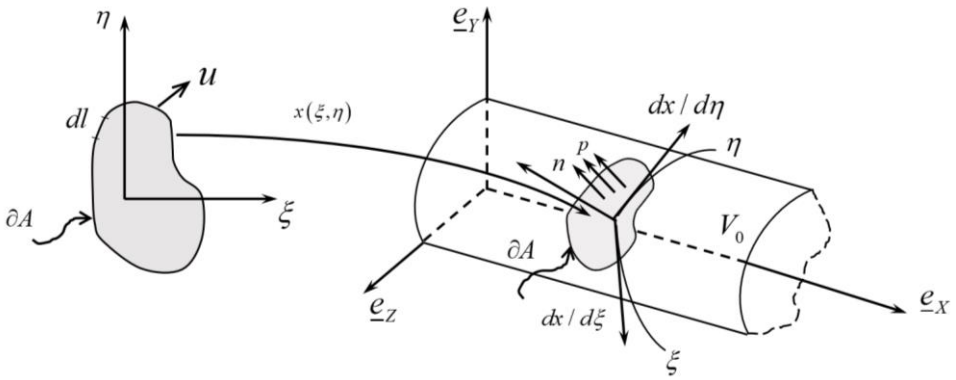

Figure 3.3 Uniform pressure on the cylindrical surface.

To determine the pressure virtual work δW_{cyl}^{p}, the curvilinear coordinates (ξ,η) are used (**Figure 3.4**):

$$\begin{cases}\xi = R_o\alpha \\ \eta = X\end{cases} \tag{3.30}$$

where α is the polar angle between the normal $\underline{\mathbf{n}}$ at a current position $\underline{\mathbf{x}}$ and the $\underline{\mathbf{e}}_Y$. The coordinates of a material point M_o are given by

$$\underline{OM}_o = \underline{\mathbf{X}} = \begin{vmatrix} X \\ R_o\cos\alpha \\ R_o\sin\alpha \end{vmatrix} \tag{3.31}$$

The position vector at the current configuration is then given by

$$\underline{\mathbf{OM}} = \underline{\mathbf{x}} = \underline{\mathbf{X}} + \underline{\mathbf{U}} = \begin{vmatrix} X + u(X) - R_o\theta_Z\cos\alpha + R_o\theta_Y\sin\alpha \\ v(X) + R_o\cos\alpha \\ w(X) + R_o\sin\alpha \end{vmatrix} \tag{3.32}$$

By using an arbitrary parameterization of the surface as shown in **Figure 3.3**, the

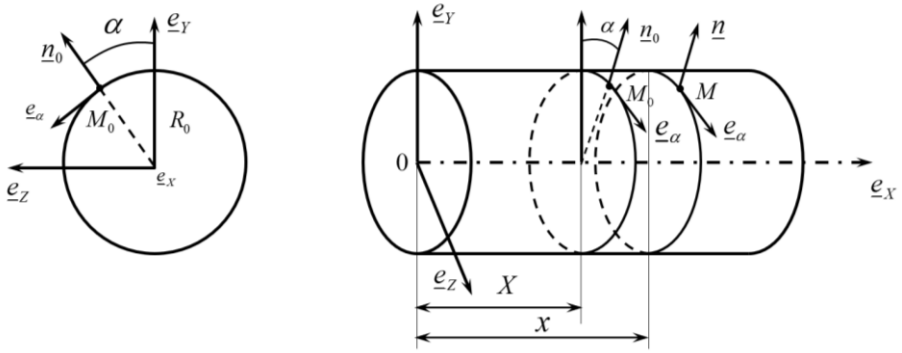

Figure 3.4 Definition of the curvilinear coordinate system.

normal and area elements can be obtained in terms of the tangent vectors $\dfrac{\partial x}{\partial \xi}$ and $\dfrac{\partial x}{\partial \eta}$ as

$$\underline{\mathbf{n}} = \frac{\dfrac{\partial x}{\partial \xi} \times \dfrac{\partial x}{\partial \eta}}{\left\| \dfrac{\partial x}{\partial \xi} \times \dfrac{\partial x}{\partial \eta} \right\|} = \frac{\dfrac{\partial x}{R_o \partial \alpha} \times \dfrac{\partial x}{\partial X}}{\left\| \dfrac{\partial x}{R_o \partial \alpha} \times \dfrac{\partial x}{\partial X} \right\|}; \tag{3.33}$$

and

$$\begin{aligned} dA &= \left\| \frac{\partial x}{\partial \xi} \times \frac{\partial x}{\partial \eta} \right\| d\xi d\eta \\ &= \left\| \frac{\partial x}{R_o \partial \alpha} \times \frac{\partial x}{\partial X} \right\| R_o d\alpha dX \end{aligned} \tag{3.34}$$

Then δW_{cyl}^{p} is:

$$\delta W_{cyl}^{p} = \int_A p.\delta \underline{\mathbf{u}} \left(\frac{\partial x}{\partial \xi} \times \frac{\partial x}{\partial \eta} \right) d\xi d\eta \tag{3.35}$$

$$= F_p \int_0^{l_o} \begin{bmatrix} -\theta_{Z,X} & \theta_{Y,X} & -w_{,X} & v_{,X} \end{bmatrix} \times \begin{Bmatrix} \delta v \\ \delta w \\ \delta \theta_Y \\ \delta \theta_Z \end{Bmatrix} dX \tag{3.36}$$

The pressure virtual work at the ends of the beam can be determined in the same way: the reference circular end surfaces ($X = 0$ and $X = l_o$) can be represented by the curvilinear coordinates $(\xi, \eta) = (r, r\alpha)$ (**Figure 3.5**). Then,

$$\delta W_{end}^{p} = \int_A p\underline{\mathbf{n}}.\delta \underline{\mathbf{u}}(l_o) dA - \int_A p\underline{\mathbf{n}}.\delta \underline{\mathbf{u}}(0) dA \tag{3.37}$$

$$= \left[\begin{bmatrix} 1 & \theta_Z(X_o) & -\theta_Y(X_o) \end{bmatrix} \times \begin{Bmatrix} \delta u(X_o) \\ \delta v(X_o) \\ \delta w(X_o) \end{Bmatrix} \right]_0^{l_o} \tag{3.38}$$

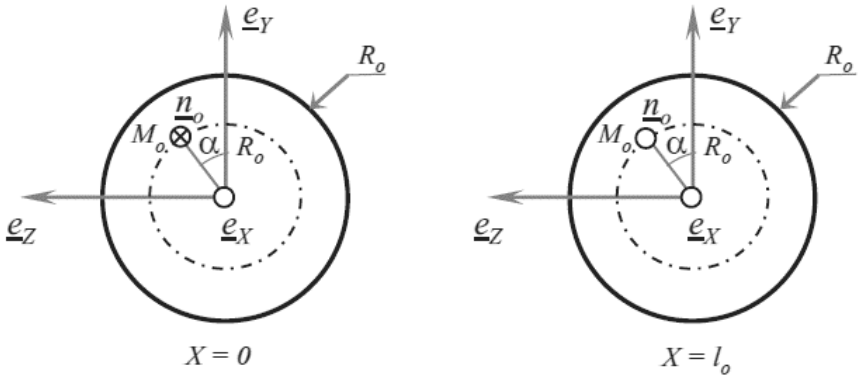

Figure 3.5 Definition of the curvilinear basis at the beam ends.

Finally, from **Eq. 3.35** and **Eq. 3.37** δW_{ext}^{p} is given by

$$\delta W_{ext}^{p} = F_p \int_0^{l_o} \begin{bmatrix} -\theta_{Z,X} & \theta_{Y,X} & -w_{,X} & v_{,X} \end{bmatrix} \times \begin{Bmatrix} \delta v \\ \delta w \\ \delta\theta_Y \\ \delta\theta_Z \end{Bmatrix} dX$$

$$= \left[\begin{bmatrix} 1 & \theta_Z(X_o) & -\theta_Y(X_o) \end{bmatrix} \times \begin{Bmatrix} \delta u(X_o) \\ \delta v(X_o) \\ \delta w(X_o) \end{Bmatrix} \right]_0^{l_o} \qquad 3.39$$

where $F_p = p\Pi R_o^2$ is the pressure force due to the inflation pressure.

One can note that, according to **Eq. 3.39**, the follower force effect of the external load due to the inflation pressure depends on the displacements and the rotations.

3.4 Conclusion

An analytical approach to approximate the critical load for an HOWF 3D Timoshenko beam was proposed in this chapter. The total Lagrangian form of the virtual work principle and Timoshenko kinematics were used to derive the beam's governing equations. By solving these linearized equations, an analytical expression of the critical buckling load was obtained.

By taking into account the orthotropic character in the present model, the study pointed out that only the mechanical properties E_l and G_{lt} intervene explicitly in the solution of critical load through C_{11} and C_{66} while Et intervenes implicitly through the reference dimensions of the beam. Only the level of orthotropy of the fabric causes noticeable discrepancies in the buckling behavior of the inflating beam. This comes from the inequality of the mechanical properties in the yarn directions. The differences between the models studied also come from the way of the establishment of the constitutive equations. In Le van's model, the material is assumed to be hyper-elastic isotropic and obeying the Saint Venant-Kirchhoff law in which only SXX and SYY are considered. The Young modulus E is also used directly in the Hookean stress-strain relationship. In the present model, we consider all components of the second Piola-Kirchhoff tensor. The elasticity tensor with the tensor components described the mechanical properties of the orthotropic material is used instead of the Young modulus E..

CHAPTER 4: FINITE-ELEMENT BUCKLING ANALYSIS OF INFLATABLE COMPOSITE BEAMS

4.1 Introduction

Analysis of finite elementinganalyses about inflating fabric structures present that challenging on both material and geometric nonlinearitie arises due to the nonlinear load, deflection behavior of the fabric, stiffening pressure of the inflating fabric, fabric-tofabric contact, and fabric wrinkling on the structural surface. To

checking fabric loads, in addition, the finite elementing model is used to predict fundamental mode of the inflating fabric beam.

4.2 Finite element model of inflatable composite beams

4.2.1 Linear eigen buckling

An expression for the strain energy of a finite inflatable beam is:

$$U_e = \frac{1}{2}\int_{V_o}\left\{\left(\underline{\underline{\mathbf{S}}}^0\right)^T \underline{\underline{\mathbf{E}}} + \underline{\underline{\mathbf{E}}}^T.\underline{\underline{\underline{\underline{\mathbf{C}}}}}.\underline{\underline{\mathbf{E}}}\right\}dV_0 = U_m + U_b \qquad 4.1$$

$\underline{\underline{\mathbf{S}}}^{\mathbf{0}}$ Inflation pressure prestressing tensor

$\{\mathbf{F_{ref}}\}$ Beam initial stress stiffness matrix

$[\mathbf{k}_\sigma]$ Element initial stress stiffness matrix

$[\mathbf{k}]$ Beam conventional elastic stiffness matrix

$\frac{1}{2}\underline{\underline{\mathbf{S}}}^T\underline{\underline{\mathbf{E}}}$. The strain energy of the beam per unit volume is

Integrating through the volume of the beam with respect to the cross-sectional area A_o and the length l_o.

where U_m and U_b is membrane changing energy and the strain bending energy, sequently.

To derive the element stiffness matrix for the beam, a displacement field $[u]=(u,v,w,\theta_Y,\theta_z)$ needs to be interpolated within each element. For the use of element for inflating beam, it is noted that the two-noded element often used for Euler-Bernoulli kinematics with Hermite polynomial as shape functions [69] Bhatti, M. (2006), or a higher order element such as the three-node quadratic beam with reduced integration [129] Le van, A. and Wielgosz, C. (2007) or the three-nodeTimoshenko beam that has quadratic shape functions for transverse displacement and linear shape functions for bending rotation and axial displacement [51] Davids, W.G. (2007); [52] Davids, W.G. and Zhang, H. (2008). In this recent analysis, the three-node Timoshenko beam element is used with C0-type continuity.

Element has three nodes with five degrees of freedom (DOF) per node. The DOF {d} defines DOF vector of an element. That is,

$$\begin{Bmatrix} u \\ v \\ w \\ \theta_Y \\ \theta_Z \end{Bmatrix} = \begin{Bmatrix} \sum_{j=1}^{3} N_j u_j \\ \sum_{j=1}^{3} N_j v_j \\ \sum_{j=1}^{3} N_j w_j \\ \sum_{j=1}^{3} N_j \theta_{Yj} \\ \sum_{j=1}^{3} N_j \theta_{Zj} \end{Bmatrix} = [N]\{d\} \qquad 4.2$$

where index j in summations runs from 1 to 3 for three-noded element, and [**N**] the shape function matrix. For the chosen element, the shape function matrix which can be found in [95]Dhatt, G., Touzot, G., and Lefrançois, E. (2005, 2007) is

$$[N] = \lfloor N_1 \quad N_2 \quad N_3 \rfloor = \left\lfloor \frac{1}{2}\xi(\xi-1) \quad 1-\xi^2 \quad \xi(\xi+1) \right\rfloor \qquad 4.3$$

where ξ is simply the dimensionless axial coordinate $\xi = \left(\frac{2}{l_0^e} X - 1 \right)$, with $\xi \in [-1,1]$ and X is the local coordinate along the beam element axis $\left(X \in \left[0, l_0^e\right] \right)$, l_0^e is the reference length.

The strain energy component U_m of the beam is associated with the stress stiffness matrix $[\mathbf{k}_\sigma]$ and U_b relates to the conventional elastic stiffness $[\mathbf{k}]$ of the beam, as

$$U_m = \frac{1}{2}[\mathbf{d}^T][\mathbf{k}_\sigma][\mathbf{d}]$$

$$U_b = \frac{1}{2}[\mathbf{d}^T][\mathbf{k}][\mathbf{d}] \qquad 4.4$$

Applying the discretization procedure, we have:

$$U_e = \frac{1}{2}\{\mathbf{d}\}^T \left([\mathbf{k}] + \lambda [\mathbf{k}_{ref}] \right) \{\mathbf{d}\} \qquad 4.5$$

where λ is the proportionality coefficient such as $F = \lambda F_{ref}$, and axial load F.

The two matrix coefficients $[\mathbf{k}]$ and $[\mathbf{k}_{ref}]$ are constant and dependent on the geometry, material properties and the inflation pressure prestressing conditions acting on the beam.

In this study, the stiffness matrix are evaluated using the Gauss numerical integration scheme. The element stiffness matrix assembly for entire structure leads to the equilibrium matrix equation in global coordinates. The potential energy of the whole beam is simply summarizing the potential energies of the individual finite elements. A whole structural matrix is generated by following the standard FEM assembly procedure.

The potential energy of whole structure can be expressed as

$$U = \frac{1}{2}\{\mathbf{D}\}^T \left([\mathbf{K}] + \lambda [\mathbf{K}_{ref}] \right) \{\mathbf{D}\} \qquad 4.6$$

The vector $\{D\}$ includes DOF for whole beam due to the problem of presumed linear. The conventional stiffness matrix $[K]$is unchanged when loaded. Let buckling displacements $\{\delta D\}$ take place relative to displacements $\{D\}$

Let buckling displacements $\{\delta \mathbf{D}\}$ take place relative to displacements $\{\mathbf{D}\}$ of the reference configuration. The structural equilibrium equations can be obtained by applying the principle of minimum potential energy. This is expressed in in the form of eigenvalue problem:

$$\left(\left[\mathbf{K}\right]+\lambda_i\left[\mathbf{K}_{ref}\right]\right)\left\{\delta\mathbf{D}\right\}=0 \qquad 4.7$$

Eq. 4.7 is an eigenvalue problem where λ_i is the eigenvalue of first buckling mode. The smallest root λ_{cr} defines the smallest level of external load for which there is decomposing named:

$$\left\{\mathbf{F}\right\}_{cr}=\lambda_{cr}\left\{\mathbf{F}\right\}_{ref} \qquad 4.8$$

As the beam is loaded by an arbitrary reference level of external load $\left\{\mathbf{F}\right\}_{ref}$, the eigenvector $\left\{\delta\mathbf{D}\right\}$ associated with λ_{cr} is the buckling mode. The magnitude of $\left\{\delta\mathbf{D}\right\}$ is indeterminate in a linear buckling problem, so that it defines a speccified shape but not an amplitude.

4.2.2 Nonlinear buckling

The axial load at i^{th} increment is calculated by

$$\left\{\mathrm{f}_i\right\}=\left\{\mathrm{f}_{i-1}\right\}+i\left\{\Delta\mathrm{f}\right\} \qquad 4.9$$

For a given element, the nonlinear equilibrium equation can be formulated as

$$\left[k_T\right]\left\{\Delta d\right\}=\left\{\mathrm{f}_i\right\} \qquad 4.10$$

Where $\left[k_T\right]$ is symbol of element tangent stiffness matrix, $\left\{\mathrm{f}_i\right\}$ and $\left\{\Delta d\right\}$ are typically the external load increments vector of an element and an unknown displacement increment to be solved. After all the elements are assembling in the model, the below equi- librium equation is shown:

$$\left[K_T\right]\left\{\Delta D\right\}=\left\{F_i\right\} \qquad 4.11$$

Eq. 4.11 can be interpreted by an incremental scheme based on the straightfoward Newton using nodal load increments $\left\{\Delta F\right\}$, with load correction terms and updates of $\left[K_T\right]$ after each incremental step. Here, the model displacement vector $\left\{D\right\}_i=\left\{D\right\}_{i-1}+\left\{\Delta D\right\}$, where $\left\{\Delta D\right\}$ is the unknown node displacement increment at increment step *i* and $\left\{D\right\}_{i-1}$ is the node-beam displacement vector from the previous solution step. The equilibrium solution tolerance was taken as

$$\left\|\left\{\Delta D\right\}_i\right\|=\left(\left\{\Delta D\right\}_i^T\left\{\Delta D\right\}_i\right)^{\frac{1}{2}}\le 0.0001 \qquad 4.12$$

Or

$$\left\|\left\{R\right\}_i\right\|=\left(\left\{R\right\}_i^T\left\{R\right\}_i\right)^{\frac{1}{2}}\le 0.0001 \qquad 4.13$$

With $\left\{R\right\}_i=\left\{R\left(D_{i-1}\right)\right\}=\left[K_T\right]\left\{\Delta D_i\right\}$ is the globally unbalanced residual force vector from the previous increment. As a limit point is approached, displacement increments $\left\{\Delta D\right\}$ become very large. Either a limit point or a bifurcationpoint, $\left[K_T\right]$ becomes singular.

4.2.3 Implementation of an iterative algorithm for solving the NLFEIB model

In the following section, the iterative procedure using the straight forward Newton-Raphson iteration with adaptive load stepping for solving the nodal displacement incrementation solution $\{\Delta D\}$ is summarized. Suppose that at increment $(i-1)$, one obtained an approximation $\{D_{i-1}\}$ of the solution as the residual is not zero.

$$\{R(D_{i-1})\} = \{F\} - [K(D_{i-1})]\{D_{i-1}\} \neq \{0\} \quad 4.14$$

At increment step *i*, one seeks an approximation $\{D_i\}$ of the solution such that:

$$\{R(D_i)\} = \{R(D_{i-1} + \Delta D_i)\} \approx \{0\} \quad 4.15$$

The algorithm is obtained by using the first-order Taylor series in the vicinity of $\{D_i\}$

$$\{R(D_{i-1} + \Delta D_i)\} = \{R(D_{i-1})\} + \left[\frac{\partial R}{\partial D}\right]_{D=D_{i-1}} \{\Delta D_i\} = \{0\} \quad 4.16$$

The NLFEIB model with linearized and incremental iterative schemes is implemented using MATLAB – the numerical computing package. At the finite element (FE) structural level, an iterative equation solution is also performed. During this structural loop, the incremental-iterative algorithm will be called at each material (Gaussian) point. In every loop within an incremental loading step ΔF, the beam parameters **Table 4.3** and the boundary conditions are prescribed, which are the input variables to the global level routine. The equation **Eq. 4.11** gives the output results from the global level routine. It solved iteratively inside the structural level. In the element level subroutine, each element are calculated to get tangently stiffness matrix $[K_T^e]$ and loading vectors $\{F_{\text{int}}^e\}$ and $\{F_{ext}^e\}$. The superscripts *(i,k,m)* denotes respectively the global counter during the current incremental loading step, number of elements and number of Gauss integration points,. After *i* loading step(s), the converged displacement solution $\{\Delta D_i\}$ at the current load ΔF will be utilized for providing incremental displacement to continuously take next loading step.

In material level, the convergence criterion can be defined by using **Eq. 4.12** or **Eq. 4.13**, which are expressed respectively in terms of the displacement vectors.

4.3 Isogeometric analysis finite element model

Isogeometric analysis proposed by [3]T.J.R. Hughes, J.A. Cottrell, Y. Bazilevs. (2005) using NURBS basis to construct exact geometry and finite element interpolating functions has received numerous attentions. More accurate solutions, compared with standard finite element, are usually obtained due to the higher-order continuity in the NURBS mesh. In finite element subdomain, dependent displacements, and initial geometric information could be described as follows,

$$\mathbf{s}^e = \sum_{c=1}^{nCe} R_c^e \mathbf{s}_c^e \quad 4.17$$

where $\mathbf{s}_c^e$ is displacements of control points, or control parameters in homogeneous space. nCe is number of control point per element.

In the present analysis, quadratic NURBS-based Timoshenko beam element with *C^1-type* continuity is used. The element has three control points with five degrees of freedom (d.o.f) $\begin{bmatrix} u_j & v_j & w_j & \theta_Y & \theta_{Zj} \end{bmatrix}$ at each control point.

$$\begin{Bmatrix} u \\ v \\ w \\ \theta_Y \\ \theta_Z \end{Bmatrix} = \begin{Bmatrix} \sum_{j=1}^{3} N_j u_j \\ \sum_{j=1}^{3} N_j v_j \\ \sum_{j=1}^{3} N_j w_j \\ \sum_{j=1}^{3} N_j \theta_j \\ \sum_{j=1}^{3} N_j \theta_{Zj} \end{Bmatrix} = \begin{bmatrix} N \end{bmatrix} (d) \qquad 4.18$$

where index *j* in summations runs from 1 to 3 for three-control points per element, and $\begin{bmatrix} N \end{bmatrix}$ the quadratic NURBS basis function vecor.

4.4 Numerical modelling and results

In this section, some representative analyses are carried out and the results are presented. It is noted that in all cases under consideration, the convergence study with regard to the number of elements is accomplished before extracting the results. Cantilever and simply-supported inflatable composite beams loaded by compressive concentrated *F* are investigated. The slenderness ratio is $\lambda_s = L / \rho$ where $L = \mu l_o$ is the beam effective length.

4.4.1 Linear finite element inflatable beam models (LFEIB)

The linear buckling analysis of inflatable beams under compressive concentrated load is performed to derive the critical load parameters. In order to assess the influence of the inflation pressure, the inflatable beam is pressurized. To examine the linear eigen buckling behavior, the normalized linear buckling load coefficient $\left(K_c^l = 10^5 \times \sigma_{cr} / E_{eq} \right)$ proposed by [57]Ovesy, H. R., & Fazilati, J. (2009) is introduced, in which σ_{cr} is the linear buckling critical stress of the beam and $E_{eq} = \sqrt{E_l E_t}$ is the equivalent Young's modulus of the current material [58]Paschero, M., & Hyer, M. W. (2009). The material, geometric parameters and pressure values used for LFEIB model are given in **Table 4.1**.

Table 4.1 Input parameters for modeling LFEIB model

Natural thickness, $t_\phi (m)$		125×10^{-6}
Correction shear coefficient, k_y		0.5
Boundary condition	Simply-supported	Fixed-free
Natural radius, $R_\phi (m)$	0.08	0.08
Natural length, $l_\phi (m)$	1.15	0.65
Young modulus, E (MPa)	250	250

Poisson ratio, v	0.3	0.3
Internal pressure (kPa)	p_1	10
	p_2	20
	p_3	30
	p_4	40

4.4.1.1 Simply-supported LFEIB

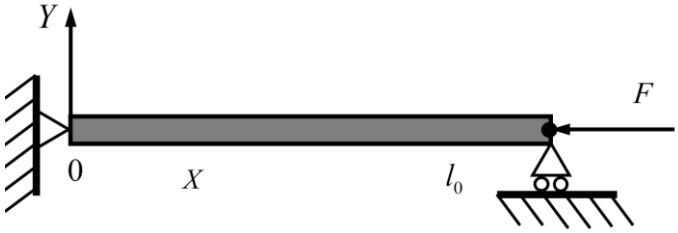

Figure 4.1 Model of a simply-supported inflatable beam subjected to axial compression load.

Figure 4.1 illustrates a cylindrical inflatable composite beam under simply-supported constrains and subjected to axial compression load. The input paremeters are presented in **Table 4.1**. Simply-supported boundary condition is assigned by,

$u = v = 0$ at $x = 0$ and $v = 0$ at $x = l_0$

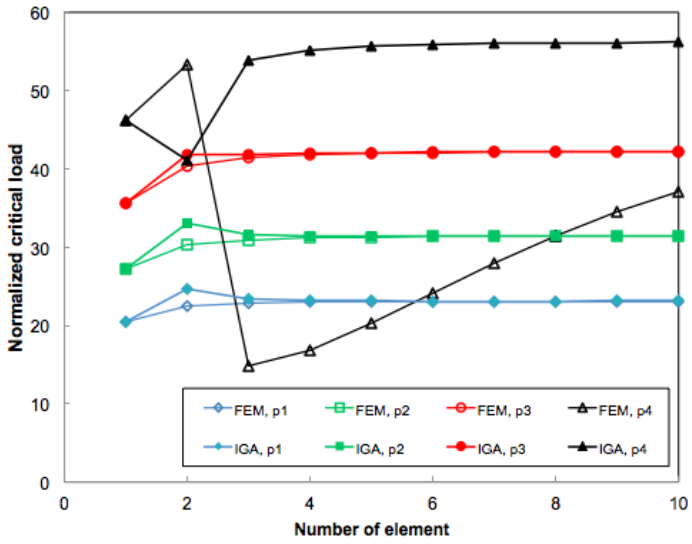

Figure 4.2 Linear eigen buckling: mesh convergence test of normalized linear buckling load coefficient $\left(K_c^l = 10^5 \times \sigma_{cr} / E_{eq}\right)$ for a simply-supported LFEIB model.

Table 4.2 Normalized critical loads K_c^l of simply-supported LFEIB inflatable beam

Pressure (kPa)	Closed-form [15]	FEM (2)	IGA (3)	Error (%)	
				(2) & (1)	(3) & (1)
10	25.31	23.11	23.12	8.69	8.65
20	33.48	31.42	31.43	6.15	6.12
30	43.27	42.22	42.22	2.43	2.43
40	54.72	31.15	56.18	43.07	2.67

4.4.1.2 Fixed – Free LFEIB

Figure 4.3 Model of a cantilever inflatable beam under axial compression load.

A cantilever LFEIB model is illustrated in **Figure 4.3**. Material and geometric properties are assumed in **Table 4.1**. Clamped boundary condition is assigned by,

$$u = v = w = \theta_x = \theta_y = 0 \text{ at } x = 0$$

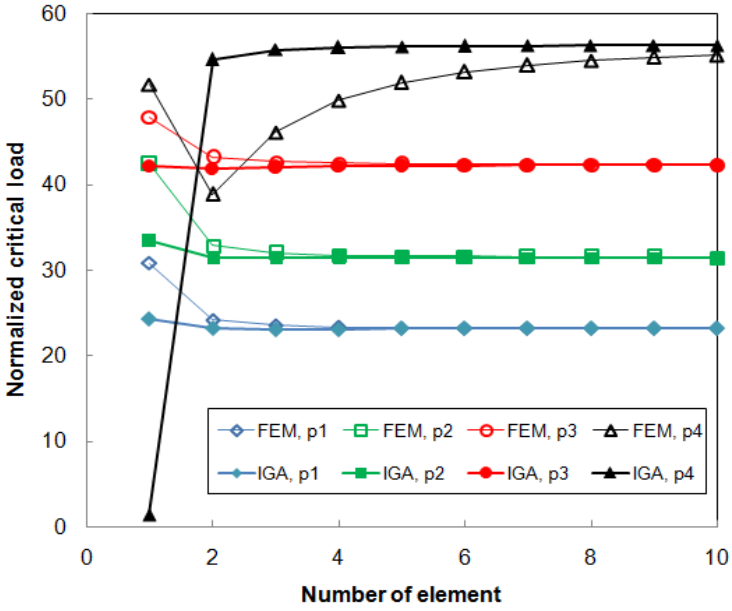

Figure 4.4 Linear eigen buckling: mesh convergence test of normalized linear buckling load coefficient $\left(K_c^l = 10^5 \times \sigma_{cr} / E_{eq}\right)$ for a cantilever LFEIB model.

4.4.2 Isogeometric nonlinear anaysis for buckling of inflatable beams

The critical load calculated in the linear buckling analysis above is appropriate only if there is little or no coupling between membrane deformation and bending. Consider the figure **Figure 4.5**, in which a small initial imperfection is introduced: either a slight initial curvature or a slight eccentricity of the compressive load F. With the increase of the initial imperfections, the beam implies large displacements rather than buckling. Hence, a linear bifurcation analysis may overestimate the actual collapse load. The normalized nonlinear load parameter at increment of axial load is defined by,

$$K_c^{nl} = 10^6 \times \frac{F_i}{E_{eq} A_0} \qquad 4.19$$

The model is made up of the material 1 and 2 as defined in **Table 4.4**. The deflection solutions D_v along Y axes obtained from the NLFEIB model are considered as the change in the flexion-to-radius ratio $\left(R_{fr}\right)$ as D_v / R_0, whereas the

axial displacement solutions D_u along *X* axes are referred to the change in the length-to-radius ratio (R_{lr}) as D_u / R_0. For the same normalized pressure and material properties, the smaller values of R_{lr} and R_{fr} represent the more stable beam.

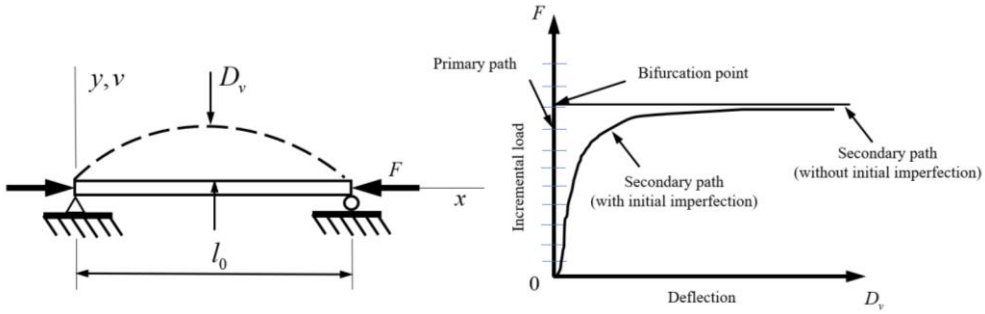

Figure 4.5 (a) Inflatable beam subjected to compressive axial load *F*. (b) The effect of an initial imperfection

Table 4.3 Input parameters for modeling NLFEIB model

Parameter type	Input	Physical interpretation	Value
Material properties	E_l	Young modulus in warp direction	See **Table 4.4**
	E_t	Young modulus in weft direction	
	G_{lt}	In-plane shear modulus	
	v_{lt}	Poisson ratio due to the loading in *l* direction and contraction in the *t* direction	
	v_{tl}	Poisson ratio due to the loading in *t* direction and contraction in the *l* direction	
Beam geometry (in the natural state)	l_ϕ	Length of the inflatable beam	See **Table 4.4**
	R_ϕ	External radius of the inflatable beam	
	t_ϕ	Thickness of the inflatable beam	
External load	p	Inflation pressure	10-200 (kPa)
	F_X	Concentrated load in *X*-axis	1500 (N)
	$\{F_i\}$	Increment load vector	
	$\{n_{inc}\}$	Number of load increments	10
Model description	n_e	Number of elements	4
	e_n	Number of control points per element	3
	n_n	Number of control points in global	$n_e + \deg$
	n_{dof}	Number degrees of freedom per node	5

e_{dof}	Number degrees of freedom per element	$e_n.n_{dof}$
g_{dof}	Number of global degrees of freedom	$n_{dof}.n_n$
m	Number of Gauss integration points	3

Table 4.4 Data set for inflatable beam

Natural thickness, $t_\phi(m)$		5×10^{-4}
Correction shear coefficient, k_y		0.5
Natural radius, $R_\phi(m)$		0.14
Natural length, $l_\phi(m)$		3
Orthotropic fabric's mechanical properties:	Material 1 (Exp.)	Material 2 (Cheng et al.(2009))
Young modulus in warp direction, E_l (MPa)	2609	19300
Young modulus in weft direction, E_t (MPa)	2994	14240
In-plane shear modulus, G_{lt} (MPa)	1171	6450
Poisson ratio, v_{lt}	0.21	0.28
Poisson ratio, v_{tl}	0.18	0.22

Table 4.5 Normalized pressure (p_n) for different values of internal pressure (p) used in the study.

	p **(kPA)**	p_n	
		Material 1	**Material 2**
p_1	10	324	43
p_2	20	648	85
p_3	30	972	128
p_4	40	1295	171

4.4.2.1 Simply-supported NLFEIB

In this problem, the nonlinear buckling of a simply supported inflating beam subjected to an axial compressive load F is investigated by the procedure proposed in **Section § 4.2.2**. The numerical examples contain large deformation analyses of NLFEIB model and illustrate the performance of the derived algorithm. A parametric study is carried out for studying the influence of normalized pressure on the NLFEIB model. At each level of normalized pressure, the corresponding crushing load $(F_{crush} = F_p)$ is the upper bound of the axial load applied to the beam. The displacements at the middle span of the beam are extracted from the global solution.

Figure 4.5 and **Figure 4.6** show the variation of flexion-to-radius ratio and length-to-radius ratio with increments of normalized load parameter K_c^{nl} in two cases of material. It is noted from the linear buckling analysis that 4 elements are sufficient to obtain converged results. At low pressure the model is unstable and therefore will fail first. At higher pressures, the R_{fr} ratio responses are quasi-linear for low increments of K_c^{nl}. The curves become nonlinear gradually at higher K_c^{nl}.

In another parametric study, the influence of the fabric properties in conjunction with the effect of the normalized pressure is pointed out. Two HOWF inflatable beams made of material 1 and 2 are considered. As mentioned in **Section § 4.4**, the nonlinear iterative solutions are obtained with inputs of normalized pressure and are normalized by two aspect ratios R_{lr} and R_{fr}.

The effects of boundary condition and material properties are clearly illustrated by the responses of simply-supported (SS) inflatable beams. In case of material 1 which has low elastic modulus than material 2, the buckling of SS beam is more sensitive at high level of internal pressure. It appears mode jump behavior when the beam withstanding increasing axial compression loads. In contrary, the distortion in load-deflection does not happen in the configuration of clamped inflatable beams.

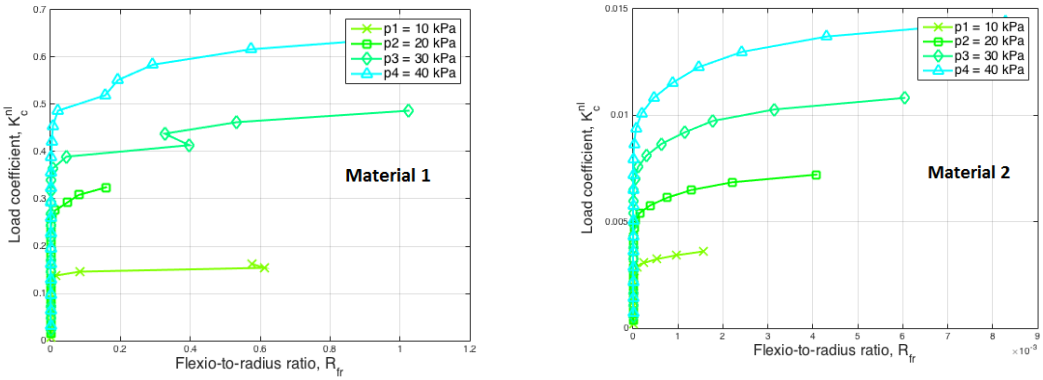

Figure 4.6 Nonlinear buckling: variation of flexion-to-radius ratio $\left(R_{fr} = D_v / R_o\right)$ with increasing normalized nonlinear load parameter $\left(K_c^{nl} = 10^6 \times F_i / \left(E_{eq} A_0\right)\right)$ for a simply supported NLFEIB model.

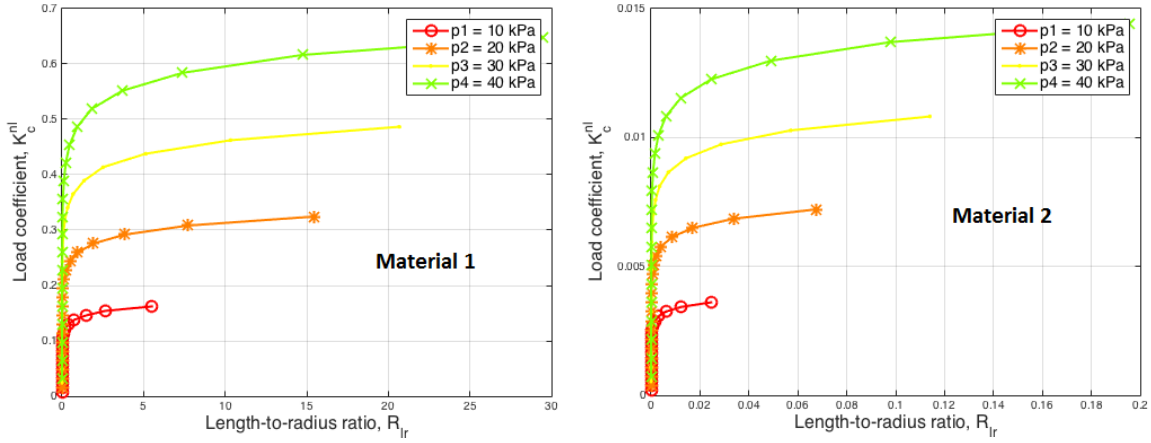

Figure 4.7 Nonlinear buckling: variation of length-to-radius ratio $\left(R_{lr} = D_u / R_o\right)$ with increasing normalized nonlinear load parameter K_c^{nl} for a simply supported NLFEIB model

4.4.2.2 Fixed-free NLFEIB

In this example, the nonlinear buckling of a cantilever inflatable beam subjected to an axial compressive load *F* is investigated. The discrepancy due to the normalized pressure between the results is clearly shown. The variation of flexion-

to-radius ratio with increments of normalized load parameter K_c^{nl} in two cases of material is given in **Figure 4.7**. Additionally, **Figure 4.8** presents length-to-radius ratio R_{lr} versus the incremental load ratio K_c^{nl}. The results show that the beam pressurized to higher pressures exhibits a better load-carrying capacity (more stable).

It is also shown that in both cases of normalized pressure, the beams made of high moduli fabric (material 2) exhibit more stability (lower values of R_{lf} and R_{fr}). The comparison between the beam response curves in two different inputs of normalized pressure also illustrates well that the beams with higher normalized pressures have the larger limits of R_{lr} and R_{fr} ratios before crushing than those with lower pressures. This is attributed to the fact that once the tows are sufficiently stressed, the inflatable beam possesses flexural stiffness capable of resisting a combination of direct compressive stress and bending.

Again, the nonliear buckling of inflactable composite beams is successfully obtained by using isogeometric analsys model. In this section, the variation of not only boundary condition but also material is taken into acount and the numerical algorithm sucessfully traced the load-deflection response of inflatable beams.

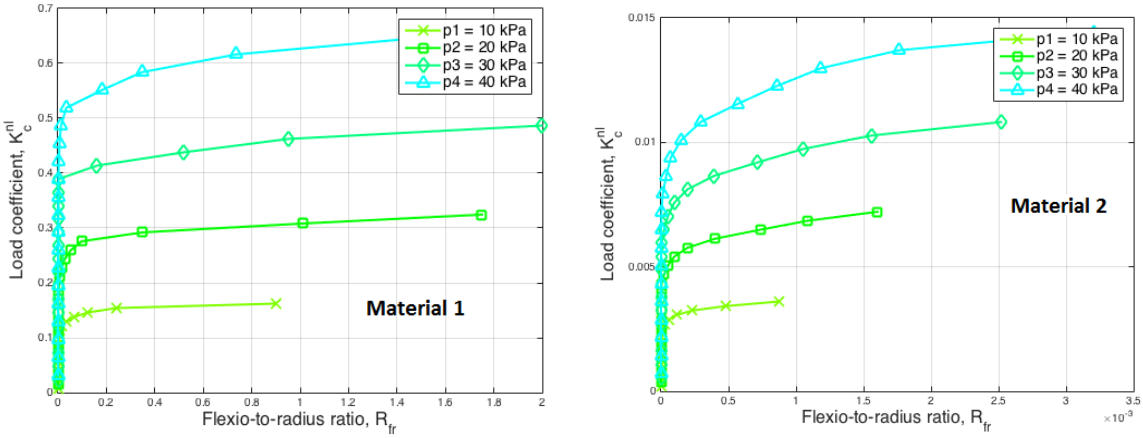

Figure 4.8 Nonlinear buckling: variation of flexion-to-radius ratio $\left(R_{fr} = D_v / R_o\right)$ with increasing normalized nonlinear load parameter $\left(K_c^{nl} = 10^6 \times F_i / \left(E_{eq} A_0\right)\right)$ for a cantilever NLFEIB model.

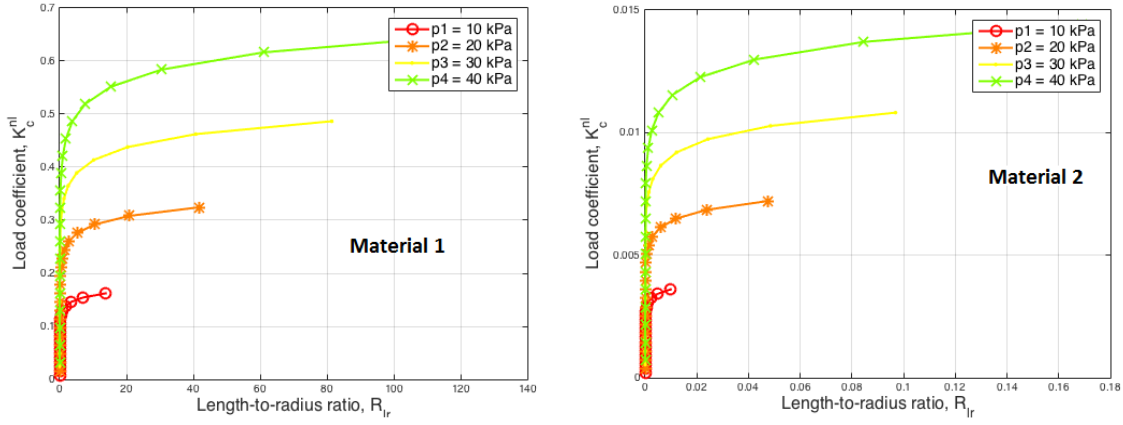

Figure 4.9 Nonlinear buckling: variation of length-to-radius ratio $\left(R_{lr} = D_u / R_o\right)$ with increasing increasing normalized nonlinear load parameter K_c^{nl} for a cantilever NLFEIB model

4.5 Conclusion

In this chapter, a linear finite element inflatable beam (LFEIB) model is proposed. A geometrically nonlinear behavior of HOWF inflatable beam made of presumed linear elastic material. A nonlinear inflatable beam finite element (NLIBFE) model is introduced. Isogeometric analysis using NURBS basis to construct exact geometry and finite element interpolating functions has received numerous attentions.

The HOWF inflating beam is analysised with C1-type continuity based on isogoemetric as well as used quadratic NURBS-based Timoshenko beam element. The element formulation is constructed by using the energy concept that the changing in membrane energy accounts and bending in strain energy are related to the stiffness matrix of the beam.

In the linear buckling analysis, a mesh convergence test on the beam critical force showed the significant improvement of the proposed numerical model in comparison with standard finite elementingmethod. The results on the buckling coefficient were also in a good agreement with those available in literature. In the nonlinear buckling analysis, the method sucessfully traced the load-deflection response of inflating beams.

Two methods FEM and IGA have been applied to verify the numerical method for the inflatable beam model. A simple beam model was simulated and calculated. The IGA method shows that building numerical models for the problem is relatively more accurate.

In future work, an analytical model and experimental program will be conducted to check the validity of the numerical solutions as a initial step of the manufacturing process that could be the base for the application of inflatable structures in Vietnam.

CHAPTER 5: BUCKLING EXPERIMENTS OF AN INFLATABLE BEAM

5.1 Introduction

This chapter presents materials selection, prototyping plan, besides also checks buckling, the relationship between load and curve by varying pressure, etc. An experimental program for buckling behavior of inflatable beams fabricated from woven fabric composites is presented in this chapter. It begins with as brief review of buckling of thin-walled shell structures, followed by the material test of woven fabric composites. Next, the fabrication procedure of inflatable beams and the buckling testing setup are described in detail. Discusion and remarks on the results obtained are then given.

5.2 Material properties and selection of fabrics

Due to real conditions in Vietnam, several fabrics types are used to make the air beams but there are not enough techinical specifications. Therefore, before the air beams are proceeding to fabricate, the mechanical properties of the selected fabrics definitely be checked.

The mechanical properties of woven fabrics are examined prior to fabricating inflatable beams. The test procedure is based on ASTM-D638/Form IV as recommended, and following steps are adopted:

Step 1: Cut dog-bone shape specimens in longitudinal and transverse directions.

Step 2: Conduct axial tensile test for determining elasic modulus and ultimate tensile strength of the fabrics.

5.2.1 The woven fabric materials

Figure 5.1 shows some of fabric composite materials available in the market which can the used for making inflatable beams. Two of them in **Figure 5.2** are widely used to make inflatable component are chosen for material tests.

The dog-bone shape coupon for tesile test has the geometric dimensions presented in **Figure 5.3** and **Table 5.2**.

Hydraulic Press Mold was employed to cut the dog-bone shape coupons. The equipment consists of a Toggle Press for Cutting Dies and Cutting Dies.

Figure 5.1 Fabric type

Figure 5.2 Waterproof PVC Laminated Tarpaulin and Coated Vinyl Fabrics

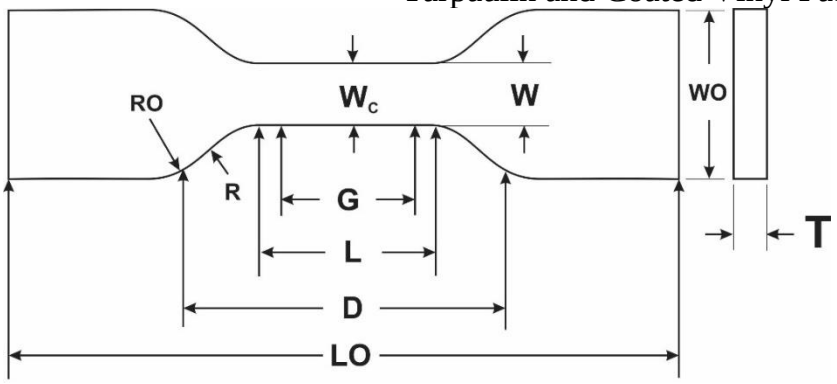

Figure 5.3 Samples after made looked like barbel

Thickness, T, shall be 0.5 ± 0.4 mm for type of molded specimen.

Table 5.1 Dimension of sample measurement

Notation	Description	Value (mm) (Type IV)
W	Section's width	6 ± 0.5
L	Section's length	33 ± 0.5
WO	Overall width	19 ± 6.4
LO	Overall length	≥ 115
G	Length measurement	25 ± 0.13
D	Distance between 2 vices	65 ± 5
R	Internal diameter	14 ± 1
RO	External diameter	25 ± 1

The dog-bone tensile test samples after cutting are shown in **Figure 5.4**. The first fabric is made of Waterproof PVC Laminated Tarpaulin, and the second fabric is made of Coated Vinyl Fabrics.

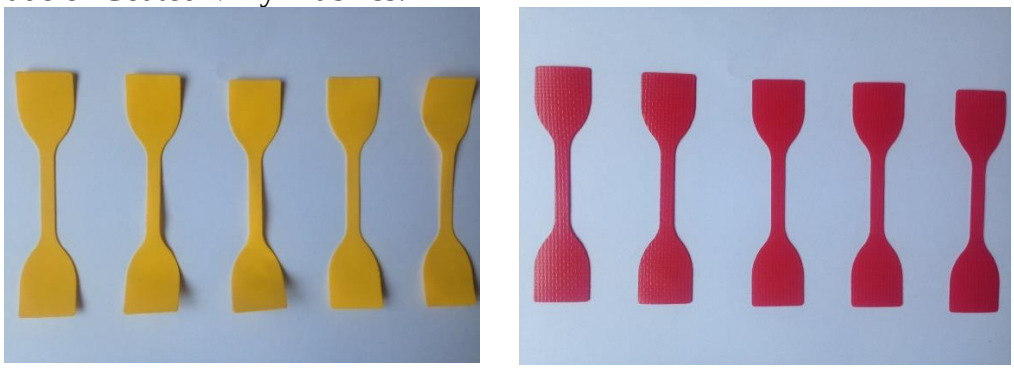

(a) (b)

Figure 5.4 Samples were cut with flat form: (a) Sample 01, (b) Sample 02

5.2.2 Mechanical properties of woven fabric composites

The tensile dog-bone samples are cut in longitudinal as well as tranverse directions. Tensile test is repeated five times for each material in each cut-direction. The test results are presented in **Table 5.2** and **Table 5.3**.

Table 5.2 Result of sample 1's longitudinal grain

No.	Maximum Load (N)	Tensile stress at Maximum Load (MPa)	Tensile extension at Maximum Load (mm)	Modulus (E-modulus) (MPa)
1	286.770	72.417	11.357	246.347
2	268.829	67.886	10.432	275.595
3	332.427	83.946	12.387	383.451
4	275.540	69.581	11.679	186.772
5	288.248	72.790	10.984	479.192
Average	290.36	73.32	11.37	314.27

Table 5.3 Result of sample 2's longitudinal grain

No.	Maximum Load (N)	Tensile stress at Maximum Load (MPa)	Tensile extension at Maximum Load (mm)	Modulus (E-modulus) (MPa)
1	149.0831	37.6473	22.9861	42.0379

2	146.6751	37.0392	22.5536	49.1538
3	137.6748	34.7664	22.7325	59.1013
4	129.7951	32.7765	22.6066	53.9681
5	131.8216	33.2883	22.3945	53.7952
Average	139.01	35.10	22.65	51.61

Figure 5.5 and **Figure 5.6 t**he relation between the axial forces and the extensions of the sample is presented in

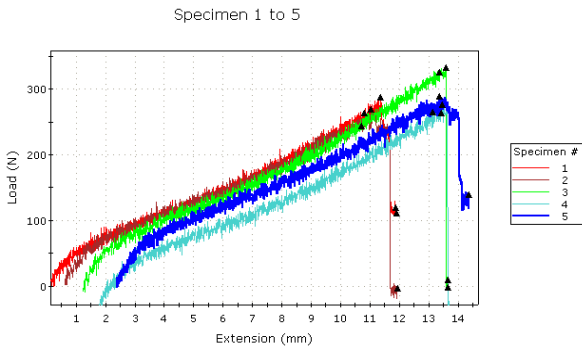

Figure 5.5 Graph of tensile strength of sample 1's longitudinal grain

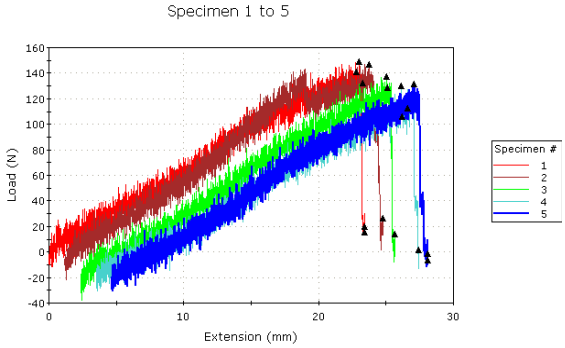

Figure 5.6 Graph of tensile strength of sample 2's longitudinal grain

Table 5.4 Result of sample 1&2's horizontal grain

	Maximum Load (N)	**Tensile stress at Maximum Load (MPa)**	**Tensile extension at Maximum Load (mm)**	**Modulus (E-modulus) (MPa)**
Average	252.81	63.84	16.89	246.06
	151.10	38.16	16.16	56.29

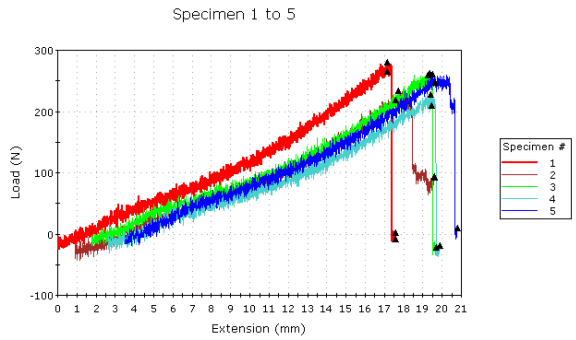

Figure 5.7 Graph of tensile strength of sample 1's horizontal grain

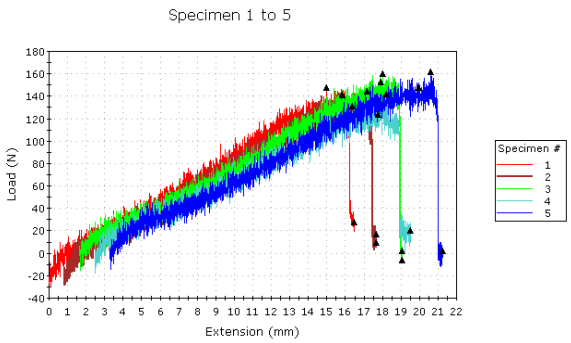

Figure 5.8 Graph of tensile strength of sample 2's horizontal grain

From the material tests, it can be seen that the first fabric has much higher tensile strengths in both longitudinal and transverse directions. Also, the leastic modula of the first (yellow) fabric in longitudinal and transverse axes are approximately five times the ones of the second (red) fabric. Therefore, the first fabric is to be the material for fabricating the inflatable beam specimens.

5.3 Test of joint's durable strength

In this study, two methods making fabric joints are investigated:

1) Glued joint.

2) Glued joint with thermal attachment.

In order to choose the proper size of the glued joint and assess the quality og the glued joint, the glued joint test samples are fabricated as in **Figure 5.9**, in which: a is the grip length, b is the original length, d is the glued length and c is the width of the joint. The actual dimensions are provided in **Table 5.5**, with d taken as 1 cm, 2 cm và 2.5 cm.

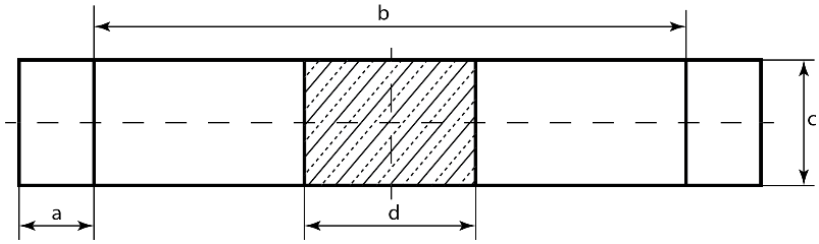

Figure 5.9 Shape of Samples: Test Specimen

Table 5.5 Sample's measurement. Sample dimensions (mm)

Distance of grip, *a*	15
Distance between of grips, *b*	$(40 \div 45) \times 2 + d$
Length of bond line, *d*	as required by each experiment
Width of specimen, *c*	25

5.3.1 Glued joint PVC 1cm

After the glued joint samples are made, the assessment of the glued joint is investigated by tensile test. Similar to the material test, the glued joint test also is taken with five samples.

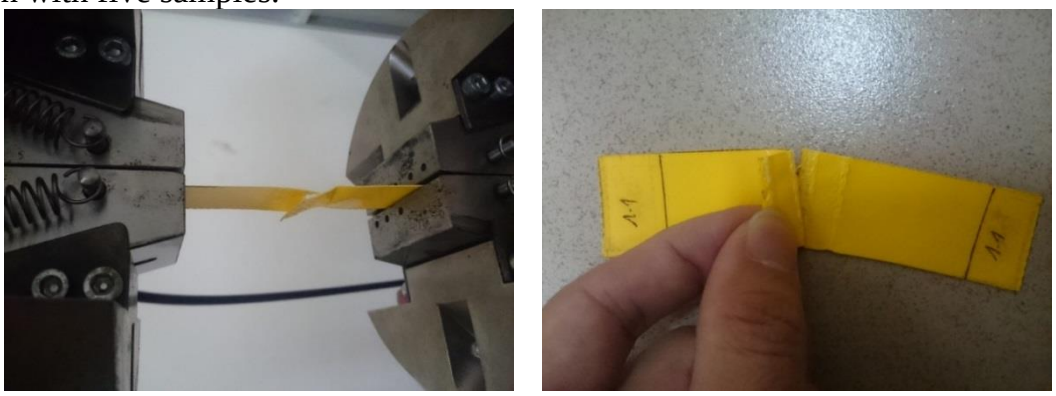

Figure 5.10 Glued joint test of 1 cm length

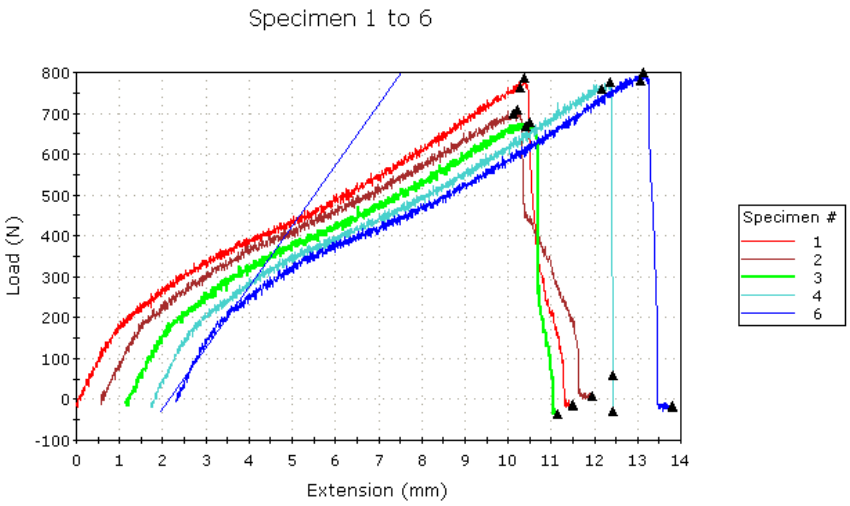

Figure 5.11 Glued joint PVC 1cm

Table 5.6 Result of Glued joint PVC 1cm

	Maximum Load (N)	Tensile stress at Maximum Load (MPa)	Tensile extension at Maximum Load (mm)	Modulus (E-modulus) (MPa)	Force/Width, N/mm
Average	731.989	24.400	9.999	214.692	731.989

5.3.2 Glued joint PVC 1cm thermal

Similar to the previous test, the glued joint PVC 1 cm thermal was also fractured at the connection as can be seen in **Figure 5.12**. Therefore, the glued joint needs to be extened.

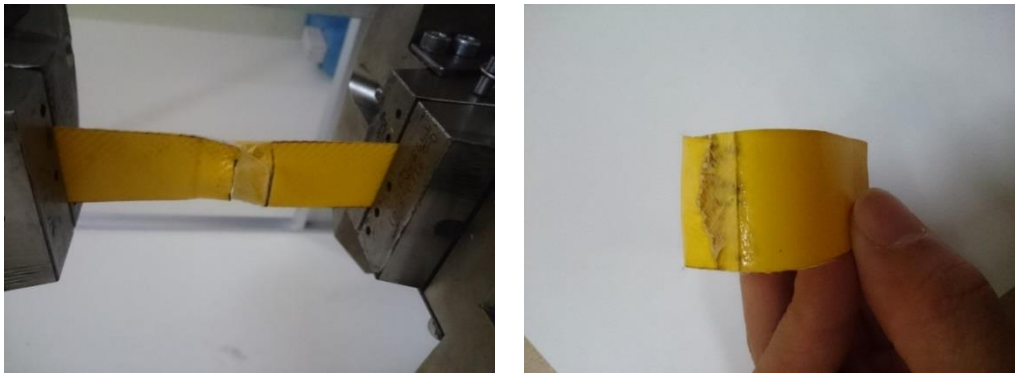

Figure 5.12 Experiment result

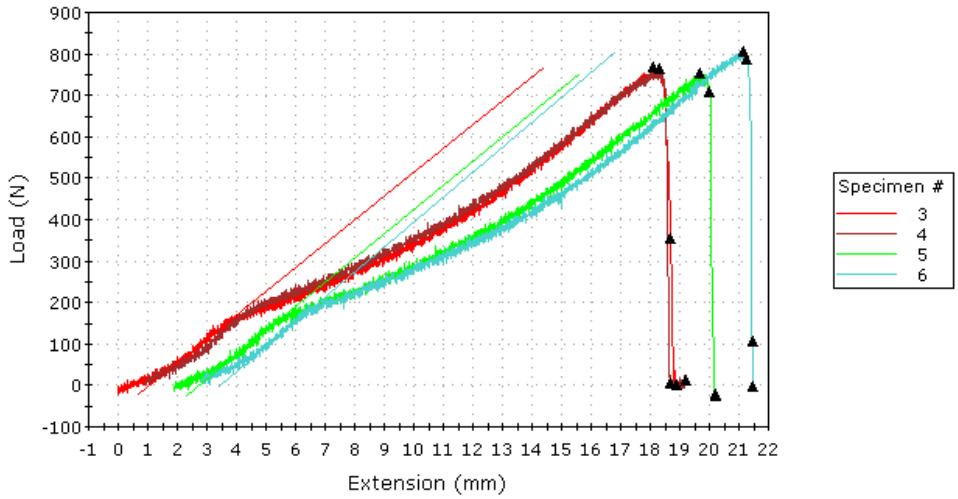

Figure 5.13 Glued joint PVC 1cm thermal

Table 5.7 Result Glued joint PVC 1cm thermal

	Maximum Load (N)	Tensile stress at Maximum Load (MPa)	Tensile extension at Maximum Load (mm)	Modulus (E-modulus) (MPa)	Force/ Width, N/mm
Average	772.831	25.761	17.890	152.200	30.913

5.3.3 Glued joint PVC 2cm thermal

For the glued joint PVC 2 cm with imposing heat, the fracture was also occurred at the connection as shown in **Figure 5.14** and **Figure 5.15** with test data provided in **Table 5.8**.

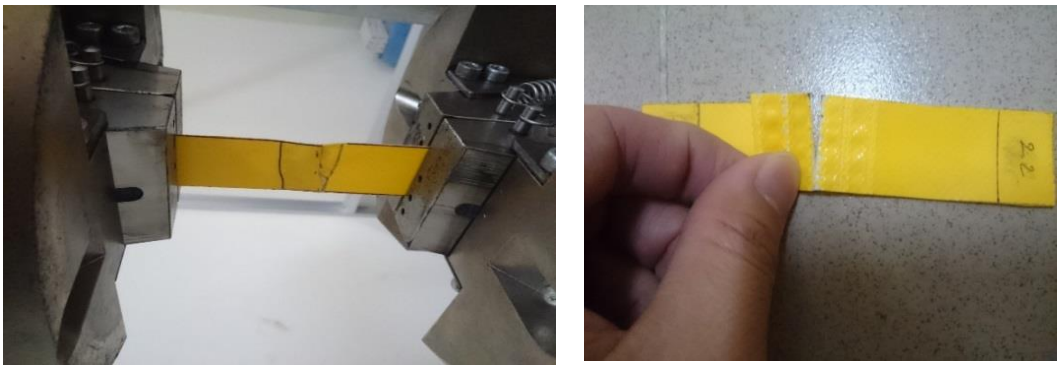

Figure 5.14 Experiment result

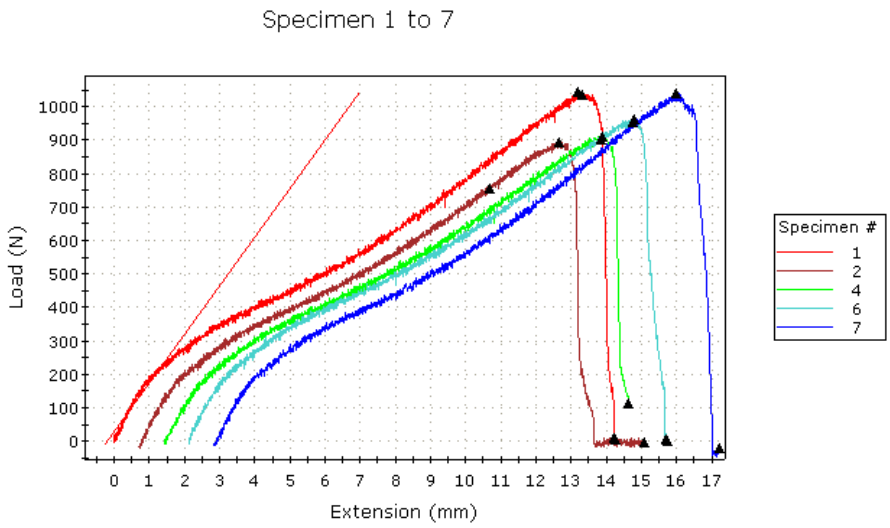

Figure 5.15 Glued joint PVC 2cm thermal

Table 5.8 Result of Glued joint PVC 2cm thermal

	Maximum Load (N)	Tensile stress at Maximum Load (MPa)	Tensile extension at Maximum Load (mm)	Modulus (E-modulus) (MPa)	Force/ Width, N/mm
Average	968.959	32.299	12.694	225.269	38.758

5.3.4 Glued joint PVC 2.5 cm with thermal attachment

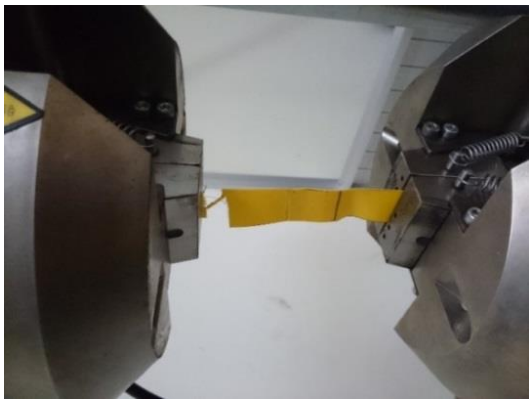

Figure 5.16 Experiment result

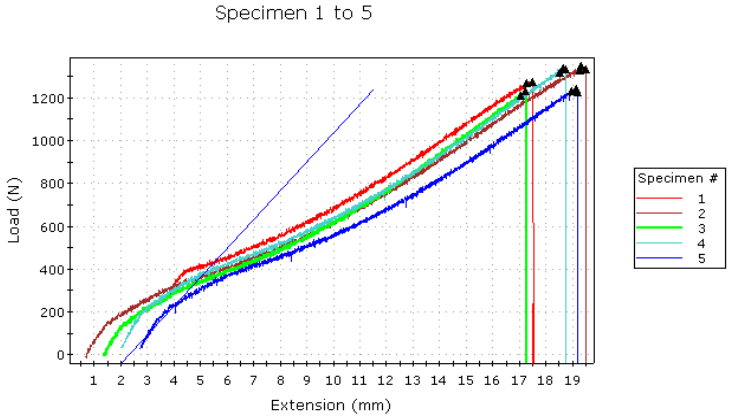

Figure 5.17 Glued joint PVC 2.5 cm thermal

Table 5.9 Result of Glued joint PVC 2.5 cm thermal

	Maximum Load (N)	Tensile stress at Maximum Load (MPa)	Tensile extension at Maximum Load (mm)	Modulus (E-modulus) (MPa)	Force/Width, N/mm
Average	1287.153	42.905	17.002	304.560	51.486

From consequence above, joints applied PVC glue and thermal attachment would improve much more when compared with the normal method (examined through force/width unit. Method using PVC glue and thermal attachment was better durable than normal one. To reinforce joint's strength, the method using PVC glue and thermal attachment (overlapped edges 2.5cm).

5.4 Inflatable beam specimens

It is necessary to depend on the available fabric sizes in Vietnamese market and experimental experiences so that it can match the initial experimental conditions.

The fabrication of specimens requires extra cares to avoid air leaking. Firstly, the beam body is constructed by joining the fabric along the length of the cylinder with the glued PVC 2.5 cm joint. To connect the cap of the beam to cylinder body is more complicated. The geometric dimnesions of the inflatable beam specimens with cylinder form has parameters as below:

Natural length: L = 200cm (excluding 2 caps at its 2 ends)

Natural outer Radius: R = 10cm

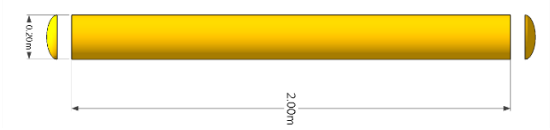

Figure 5.18 Design of inflatable beam

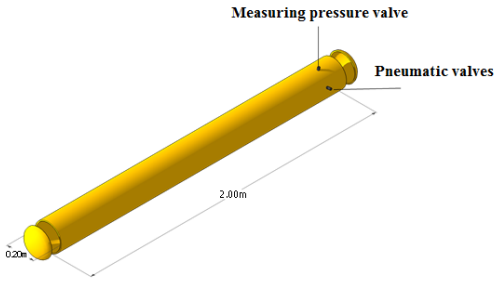

Figure 5.19 Valves of pumping and manometer

Following tensile and stick experiment's data, sample 1's material (yellow fiber) was chosen for processing design of Inflatable beam samples. Method using PVC glue and thermal pressure 2.5cm. Two caps at two ends need machining so that they are very close, glued or sewed joining area can be suffered pneumatic pressure. Therefore, deployment may run into some issues, those are joint's errors that make air leaking outside beam. Thus, sticking process must be done carefully, an amount of glue is absolutely enough, and the imposing heat must be correct so as to their unification.

Structure of 2 valves of pumping and manometer at the position 20cm from beam's end. One should be located far from another (60º-90º).

Figure 5.20 Inflatable beam after pumping

Figure 5.21 Inflatable beam's manometer

5.5 Buckling test set-up

In this study, three cylindrical inflatable beams are fabricated with the radius of R = 100mm and the length of L = 2m. A compressive load F is applied incrementally at one beam end: at first, one resets the load F to zero, and then gradually increases F. To visualize the lateral deflections of the beam during its axial compression loading, a tachometer with the precision order of 1 mm was used. The device was positioned about 4-5 m of the testing beam.

This sequence is repeated until the first wrinkles appear which is called the critical point. At this point, the load F is the critical load of the beam. After passing the critical point, the beam rigidity has decreased, the axial displacement becomes very large and the compressive load cannot be increased.

The beam is subjected to an internal pressure p first under which the beam is in a prestressing state. An external load F is applied by a winch stacker at the end in the axial direction of the beam. A schematic view of the test set-up is shown in **Figure 5.25.**

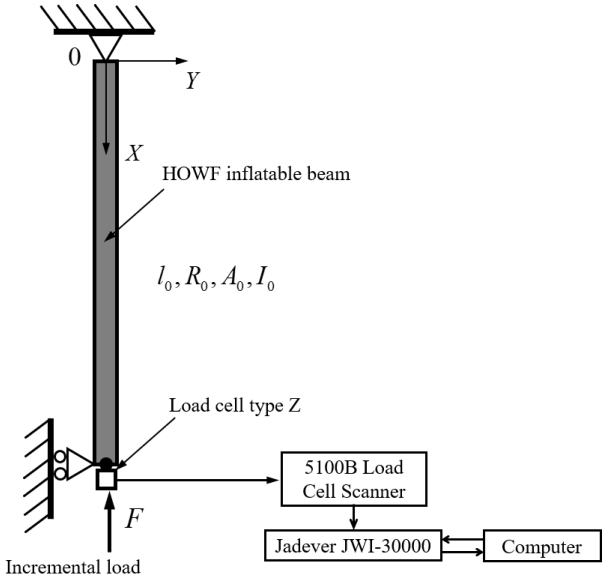

Figure 5.22 Schematic diagram of simply supported HOWF inflatable beam and instrumentation for buckling test.

Due to the apparatus limitations, the boundary conditions applied to the structure are only simply supported. The beam is mounted in a vertical chassis with two supports at two ends. The support at bottom (the load applied end) is movable in axial direction. The experimental apparatus is shown in **Figure 5.23**.

The inflatable beams having the diameter of 200 mm and the length of 2 m is inflated with the air pressure of 1 kg/cm^2 (1kPa). The air pressure is monitored via a dial gauge attached to the valve built in the beam body.

One end of the beam is fixed to the test frame and the other end is only free to move in axial direction.

The test frame

The test frame as shown in **Figure 5.23** is made of standard alluminum uprights having a fixed top end and the bottom end can move following the alluminum guide. The whole frame is attached rigidly to the wall.

Figure 5.23 Frame system

Fixed-end and pin-end supports

Fixed-end support includes an alluminum plate fixed to the frame and a adjustable ring to fit the inflatable beam. The pin-end support at the bottom is also attached to an alluminum plate and has a ring to hold the bottom end. The bottom end is attached to the uprights with roller, allowing axis displatement of the bottom end. **Figure 5.24** illustrates detail of these supports.

Instrumentation

- A load jack used to apply axial compressive load onto the beam and the load value is monitored by using a load-cell placed between the jack and the bottom alluminum plate, see **Figure 5.27**.

Linear Variable Differential Transformer (LVDT) is used to measure the axial and transverse displacements of the beam under load. The LVDT is connected to a data acquisition computer to record the displacement variable as shown in Error! Reference source not found..

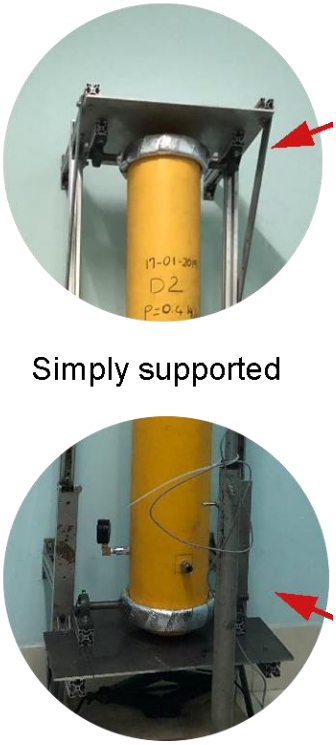

Figure 5.24 The fixed-end and pin-end support

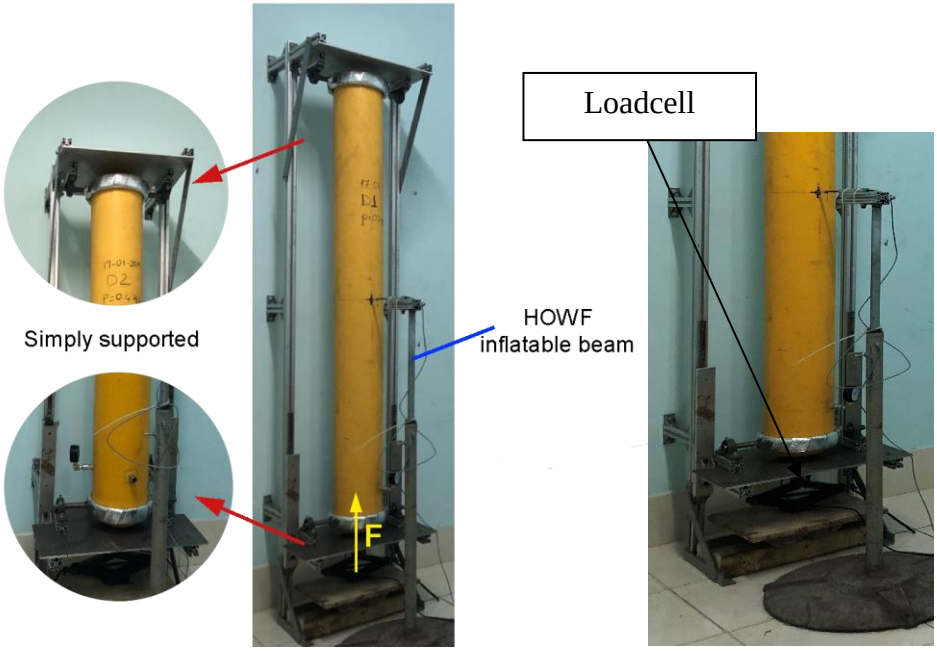

Figure 5.25 Experimental apparatus of HOWF simply supported inflatable beam for measuring the critical load

The pressure is measured twice per second and displayed by a precision digital manometer KK GAUGE (**Figure 5.26**), which can measure up to 5 bar pressure with a precision of 0.01 bar. The pressures measured are in the range of 0.1- 0.3 bar.

(a) Pressure control valve (b) Pressure gauge

Figure 5.26 Digital Manometer KK GAUGE

After setting up the measuring equipments, the beam is inflated up to a certain pressure to maintain the shape of the beam, then position the beam into the test frame. The beam is then inflated to the designed pressure. As the diameter of the beam is enlarged when increasing air pressure, the top and bottom rings need to be adjusted to fit the beam, see **Figure 5.27.**

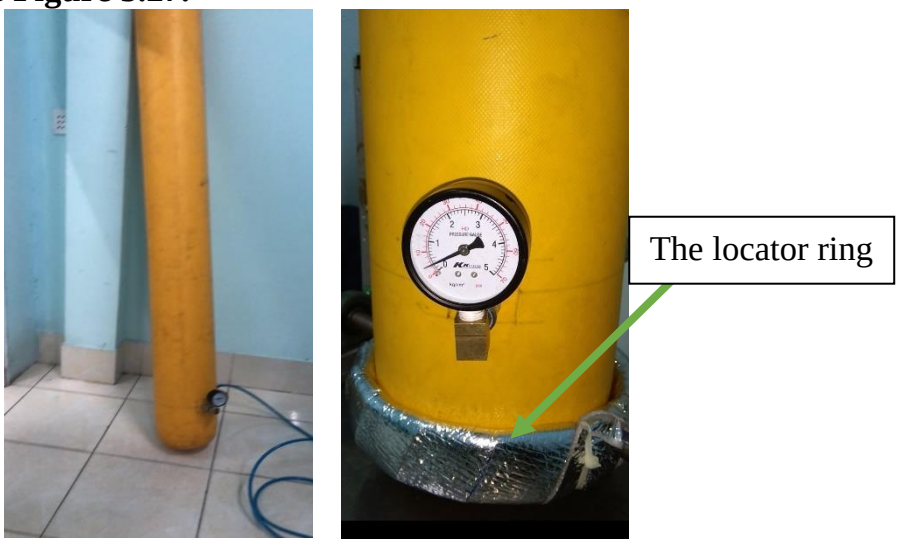

Figure 5.27 The locator ring can be adjusted in diameter

After inflating the beam, the axial compressive load is gradually applied at the bottom end. The load value is monitored via data acquisition to control the load rate. A beam specimen will be tested with four different values of air pressure, i.e. 20 kPa, 40 kPa, 60 kPa and 80 kPa. It can be seen in the **Figure 5.28** that the wrinkle appears at the same positon of the beam indepentable to the air pressure values. Therefore, it can be concluded that the wrinkle position is dependent to the beam's geometry and material properties rather than the air pressure.

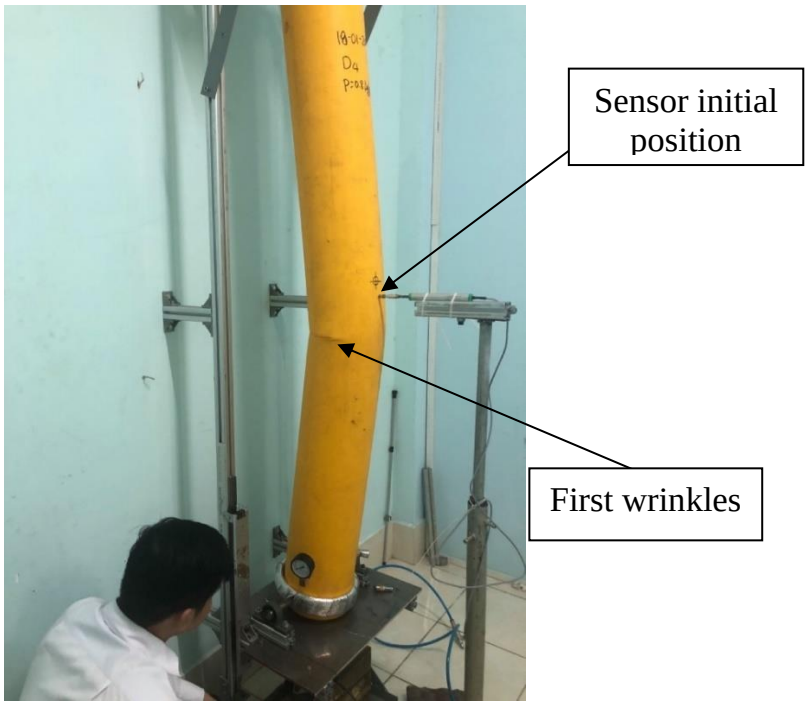

Figure 5.28 The first wrinkles appears

The first wrinkle indicates the instability configuration of the beam and the largest deflection occurs at the wrinkle position.

5.6 Experimental results and discussion

A typical test included the following steps:

1. Loading the beam until the first wrinkles of the skin appeared. Releasing the load.

2. Loading and unloading the beam above the first buckling load several times.

3. Loading the beam until collapse

Strain gages, end-shortening and lateral readings as a function of the axial compression loading were recorded at each of above step, accompanied by video recording and photographs. It is also noted that the wrinkle magnitude is proportional to the beam rigidity. The beam must be relaxed in a reasonable time between the tests for the wrinkles disappear completely.

5.6.1 Load vs displacement u relation of beam at pressure

The experimental results determine the load-displacement relation of the inflatable beams with air pressures of 20 kPa, 40 kPa, 60 kPa and 80 kPa.

We can be seen that the largest deviation is about 4.7% occuring as soon as the occurrence of the wrinkle. Such a small deviation indicates a good measurement method.

According to the **Figure 5.29 - Figure 5.32 ,** it can be seen that the axial displacement increases linearly with the applied load, and the stiffness of the beam increases with the increase of the air pressure.

The first wrinkle appears when the axial displacement being about 70 mm. The first wrinkle of the beam indicates the instablity of the beam, and soon enough the beam would buckle, leading to the significant decrease of load-carrying capacity of the inflatable beam.

The wrinkle occurs at a similar location in the beam, e.g. at the middle section. This can be explaned that the air pressure in the beam increases its load-carrying capacity, but the air pressure does not affect the buckling mode of the beam.

Each specimen is tested repeatedly four times for each air pressure magnitude. The critical load of the beam tends to be lower due to the fact that the the textile fibres have not fully recovered from the previous test. Therefore, it may be needed to investigate further into the composite material, as well as optimise the shape of the inflatable beam in order to obtain more accurate results.

a) p = 20 kPa

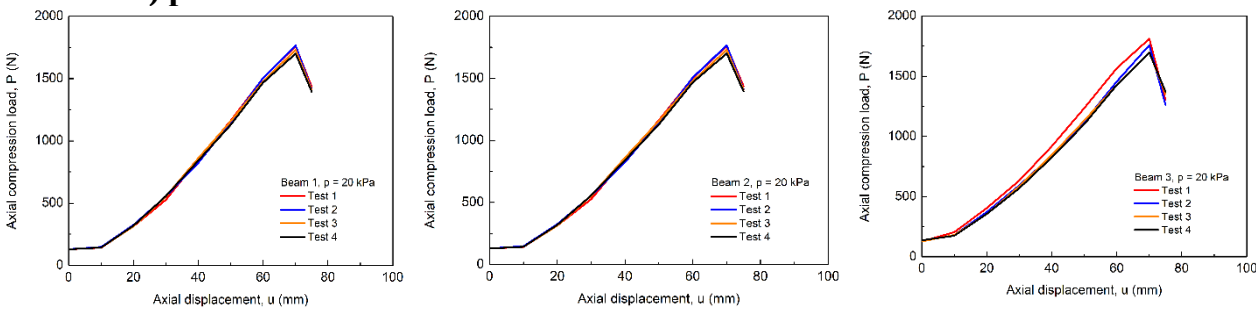

Figure 5.29 Load vs displacement relation of beam at pressure p = 20kPa.

b) p = 40 kPa

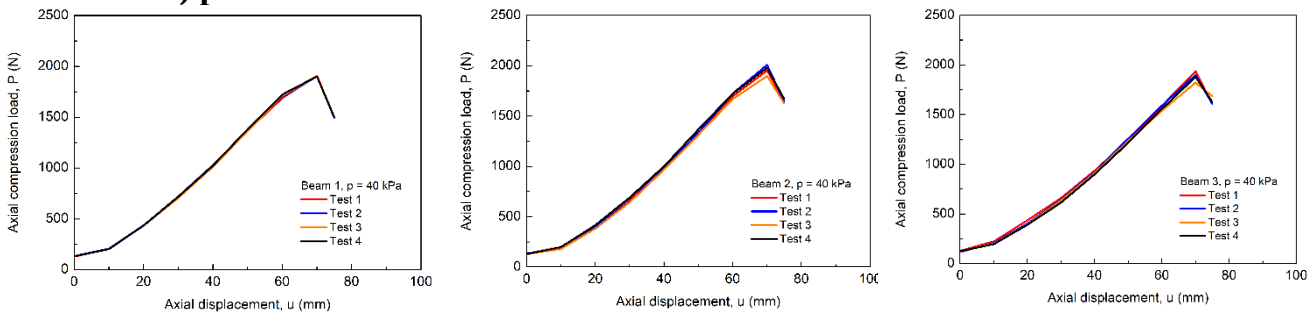

Figure 5.30 Load vs displacement relation of beam at pressure p= 40 kPa

c) p = 60 kPa

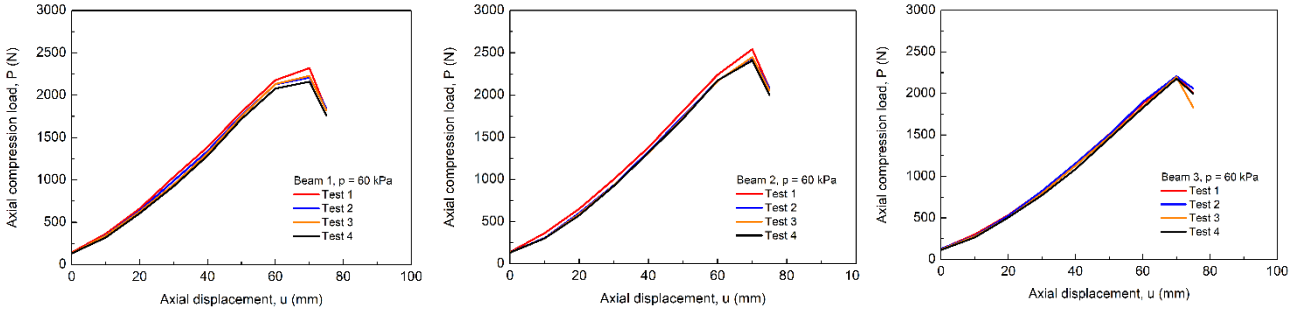

Figure 5.31 Load vs displacement relation of beam at pressure p = 60 kPa

d) p = 80 kPa

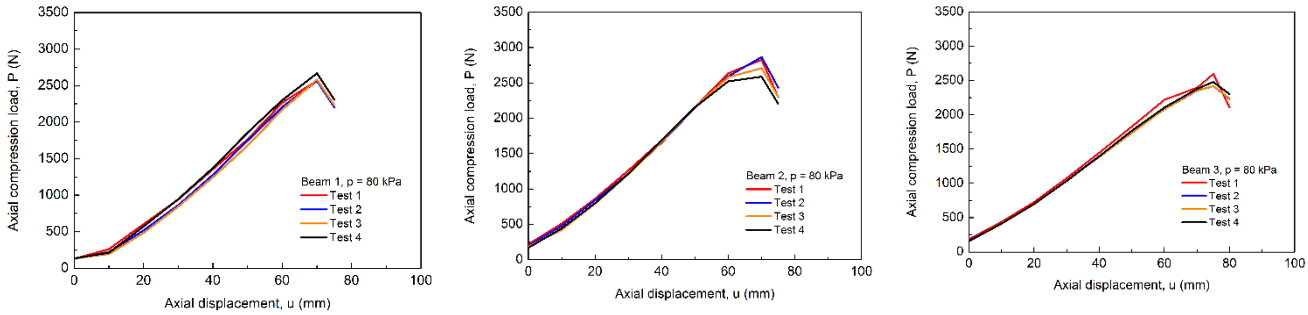

Figure 5.32 Load vs displacement relation of beam at pressure p= 80 kPa

5.6.1.1 Beams inflated with different air pressures

The following Figures shows that carrying capacity of beams depends on pressure. The pressure increases, the loading capacity typically increases.

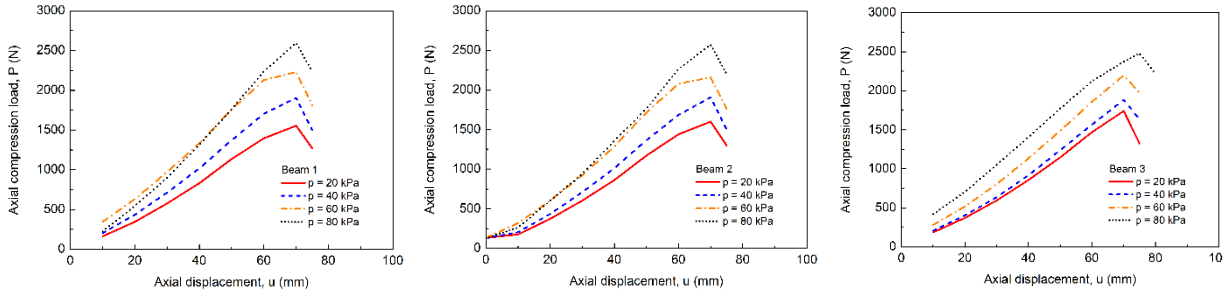

Figure 5.33 Load vs displacement relation of beam 1, 2, 3 at different pressures

5.6.1.2 Comparison of 3 beams at pressure p = 80 kPa

According to the experimental results, when the axial load-carrying capacity of the beam get higher, the air-pressure maginitude particularly increases. The highest deviation of this critical load on the beams which compared to the average value is approximately 5.85%. This result indicates the uniformity of the specimen during the fabrication process. In summary, the beams with this result are fabricated by gluing with heat method… that give a similar result.

The **Figure 5.34** compares the buckling behaviour of the inflatable beams with different pressure applied, which demonstrates that the air pressure largely affects the stability of the inflatable beam. The experiment also shows that the maximum load-carrying capacity is proportion to the applied pressure.

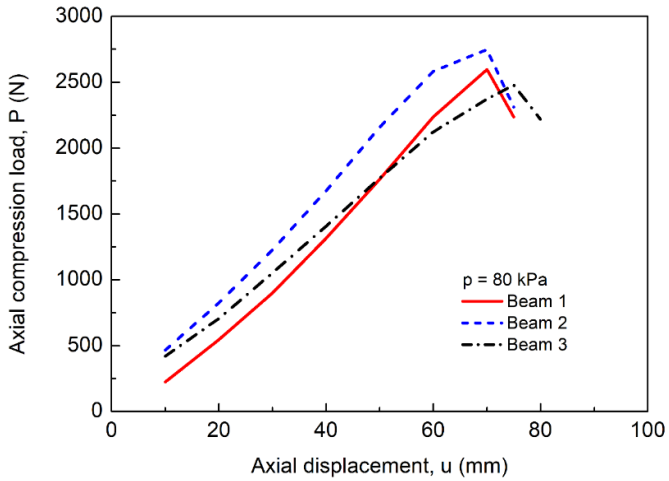

Figure 5.34 Comparison of 3 beams at pressure p = 80 kPa

5.6.2 Load vs displacement v relation of beam at pressure

To evaluate the influence of relationship between the load and displacement horizontal direction, each beam was examined respectively with pressure values of 20 kPa, 40 kPa, 60 kPa and 80 kPa. Each experiment was performed four times. Experimental results are presented in **Figure 5.35**, **Figure 5.36**, **Figure 5.37** and **Figure 5.38**. These results also show that when the pressure increases, the load capacity increase simultaneously and the displacing value before cracking also increases respectively.

a) p = 20 Kpa

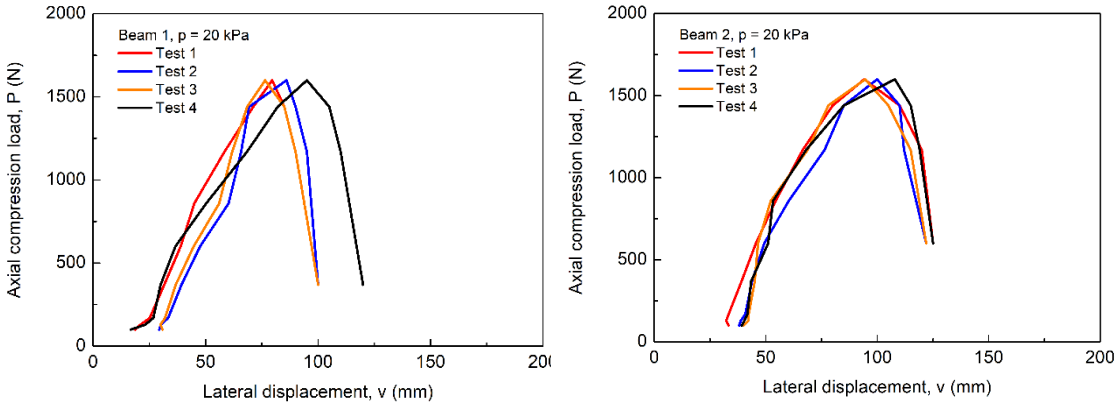

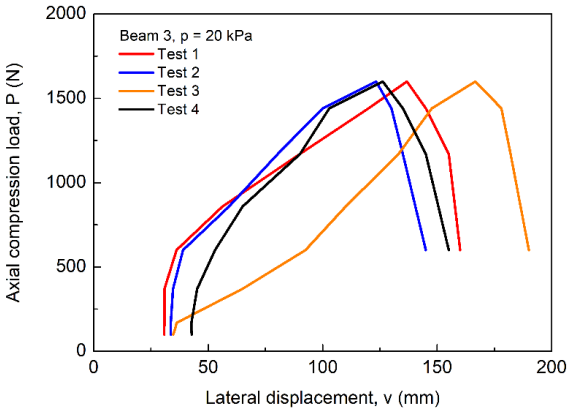

Figure 5.35 Load vs displacement relation of beam at pressure p = 20kPa

b) p = 40 Kpa

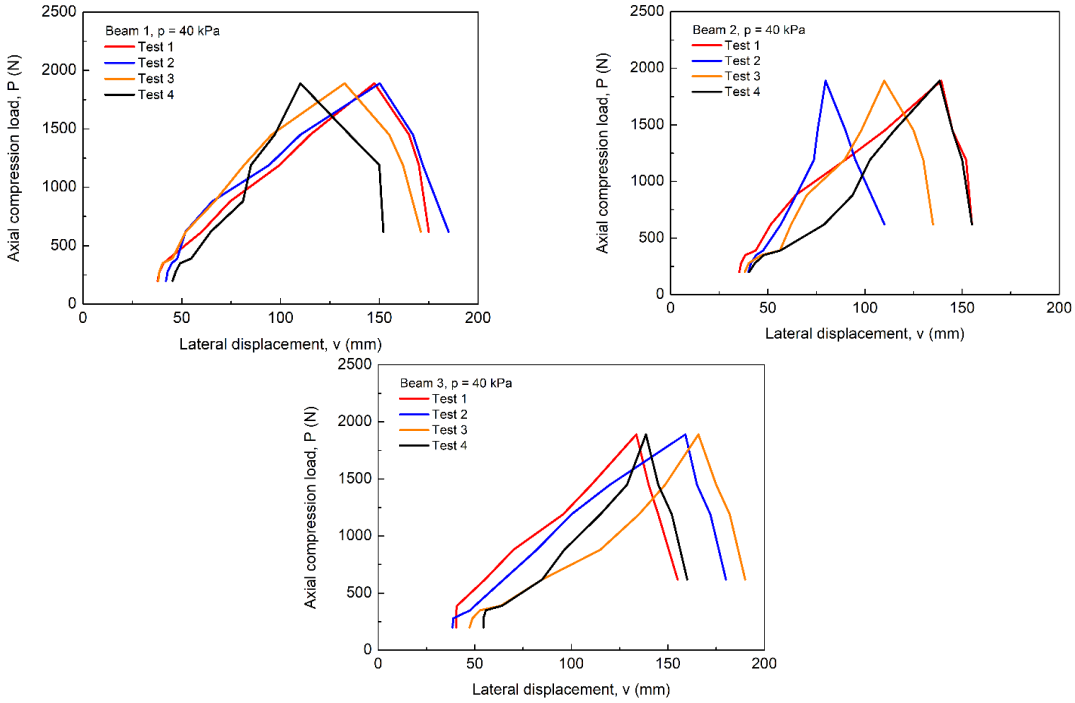

Figure 5.36 Load vs displacement relation of beam at pressure p =40 kPa

c) p = 60 Kpa

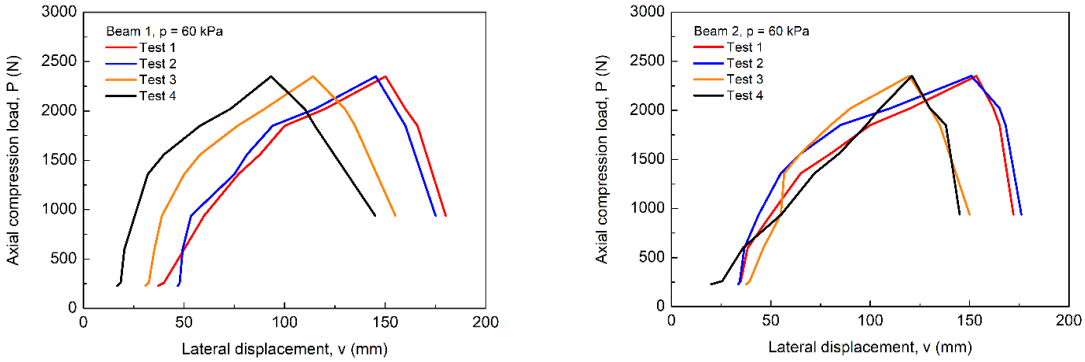

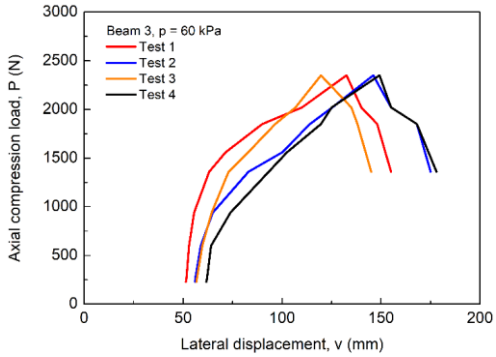

Figure 5.37 Load vs displacement relation of beam at pressure p =60 kPa

d) p = 60 Kpa

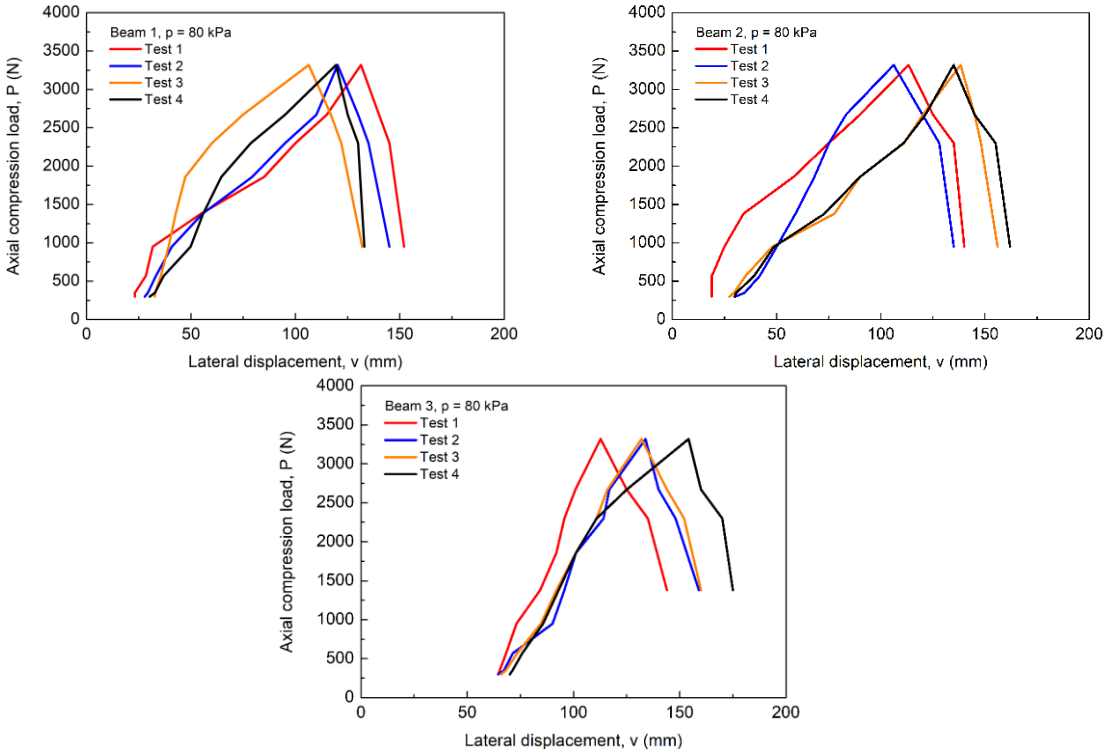

Figure 5.38 Load vs displacement relation of beam at pressure p= 80 kPa

1380 144 159 160 175 160

5.6.2.1 Beams inflated with different air pressures

The following Figures shows that carrying capacity of beams depends on pressure. The pressure increases, the loading capacity typically increases.

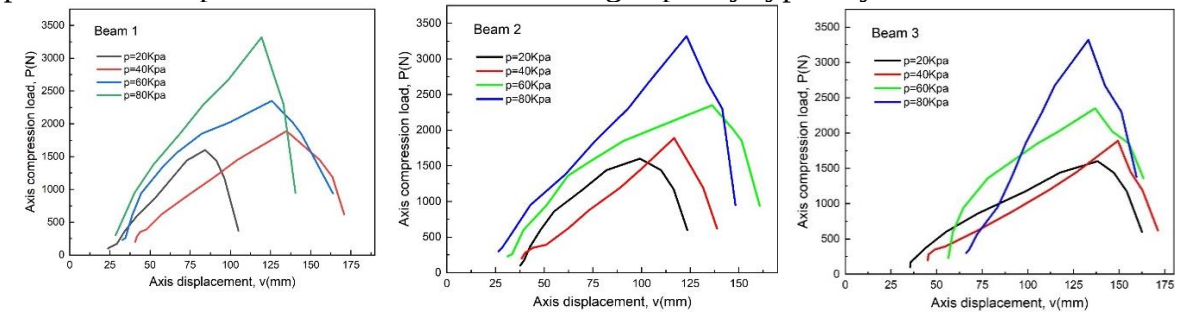

Figure 5.39 Load vs displacement relation of beam 1, 2, 3 at different pressures

5.6.2.2 Comparison of 3 beams at pressure p = 80 kN

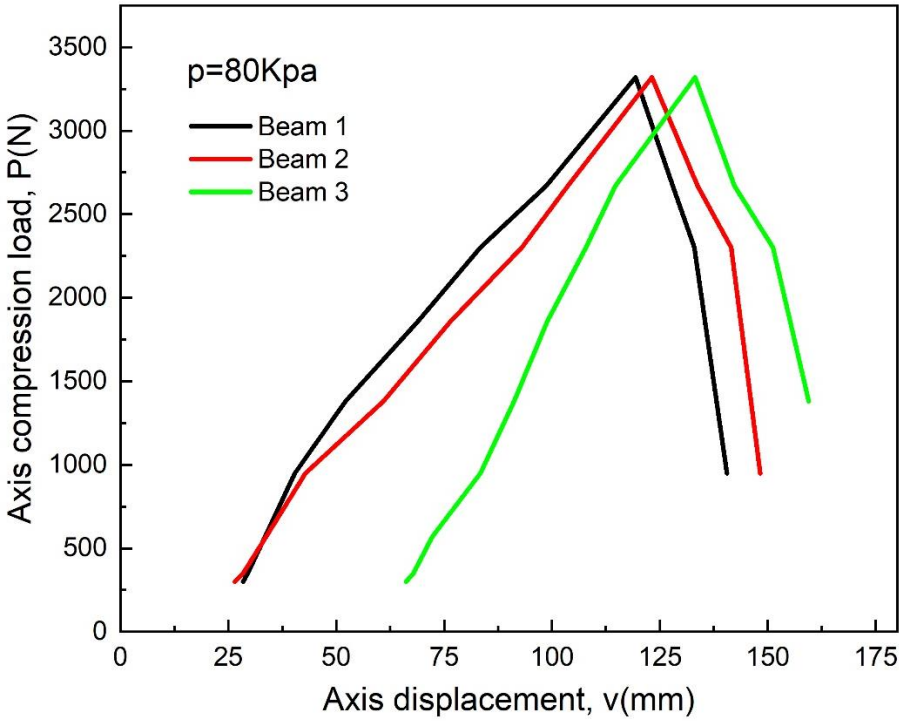

Figure 5.40 Comparison of 3 beams at pressure p = 80 kN

5.7 Comparison between experimental and IGA numerical methods

Figure 5.41 compares the experimental results and simulation results by IGA. The results show that experimental working with low pressures, the convergence is very low. However, if the pressure in the beam increases, the convergence improves significantly. This expression can be explained as follows: In the experimental process, while we inflate and conduct experiments at low pressures, the beam is not tension enough so that it can keep the beam firm at this time. We can just put the sensors in at this time and it creates settlement on the beam body. At the same time, the sensor has not received the result of compressive force during the compression process. However, the deformation according to “u” changes that make the beam radius increases. The result was that we can see initial stages of experiments, the sensors often earlier receive the results on the diagrams. However, when increasing the pump pressure in the beam, we observe that the numerical and experimental results are converged. Furthermore, the real materials also caused significant errors in the implementation.

5.7.1 IGA prediction vs Experimental results, in axial displacement u with air pressure 20 kPa, 40 kPa, 60 kPa, 80 kPa

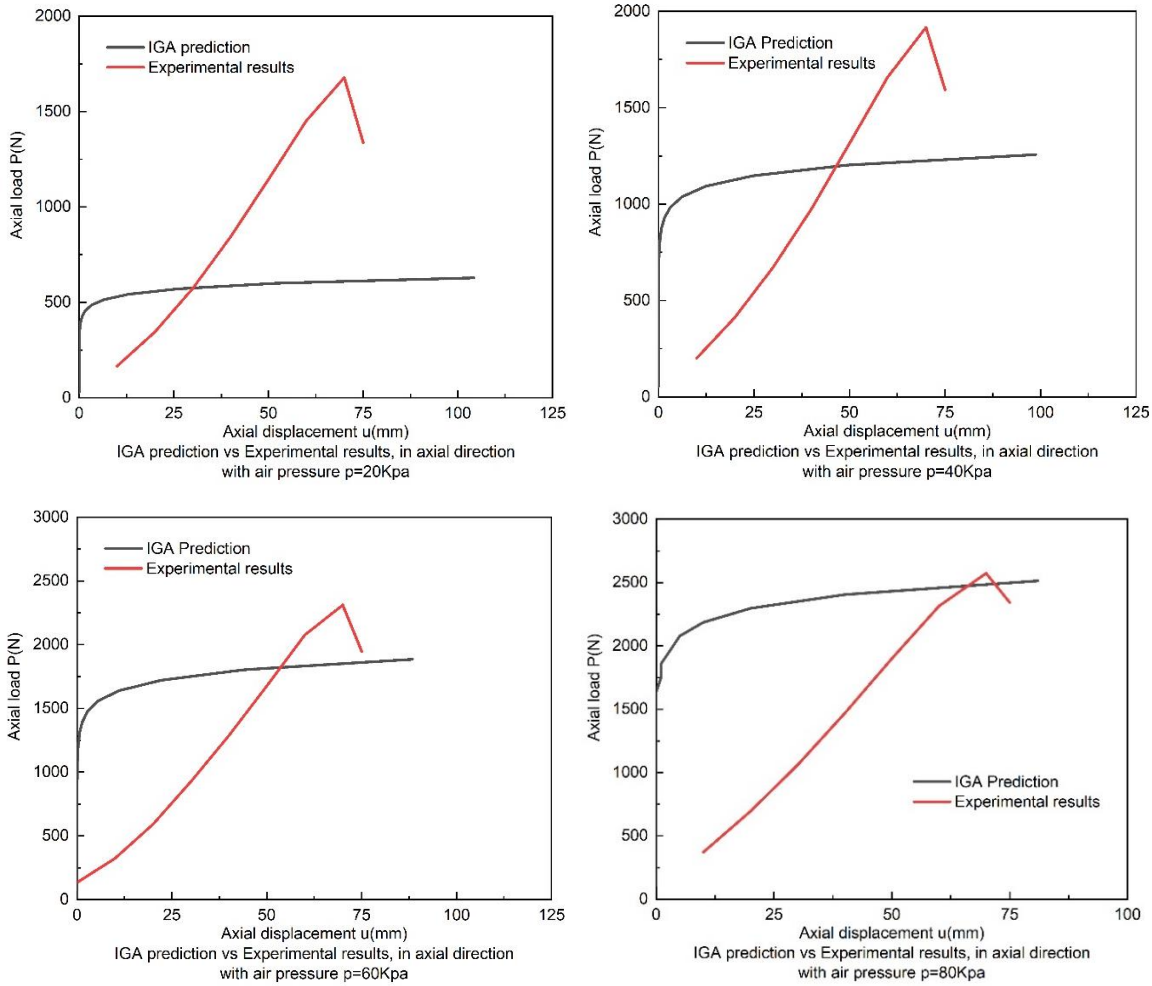

Figure 5.41 IGA prediction vs Experimental results, in axial displacement u with air pressure 20 kpa, 40 kpa, 60 kpa and 80 kpa

5.7.2 IGA prediction vs Experimental results, in transverse displacement v with air pressure 20 kPa, 40 kPa, 60 kPa, 80 kPa

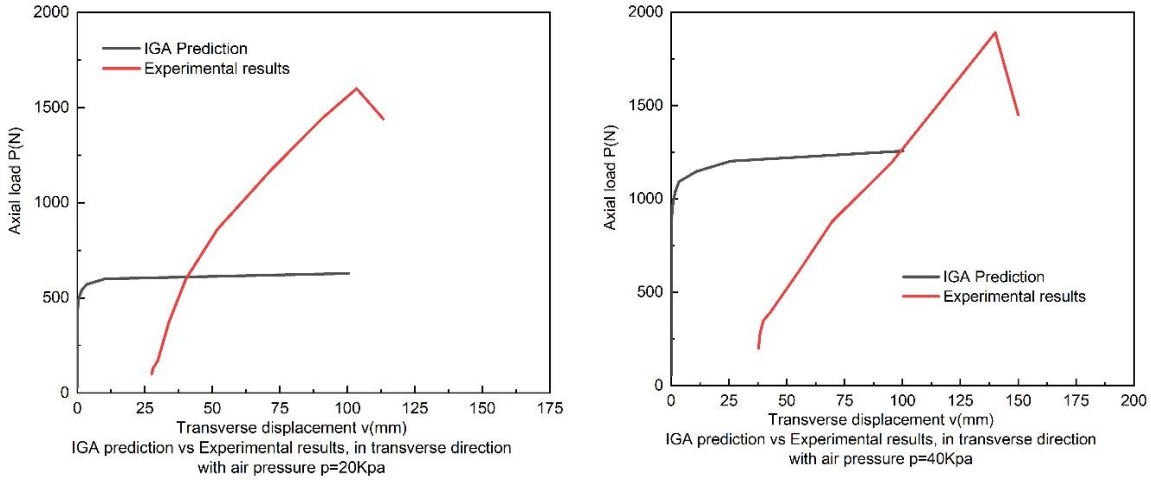

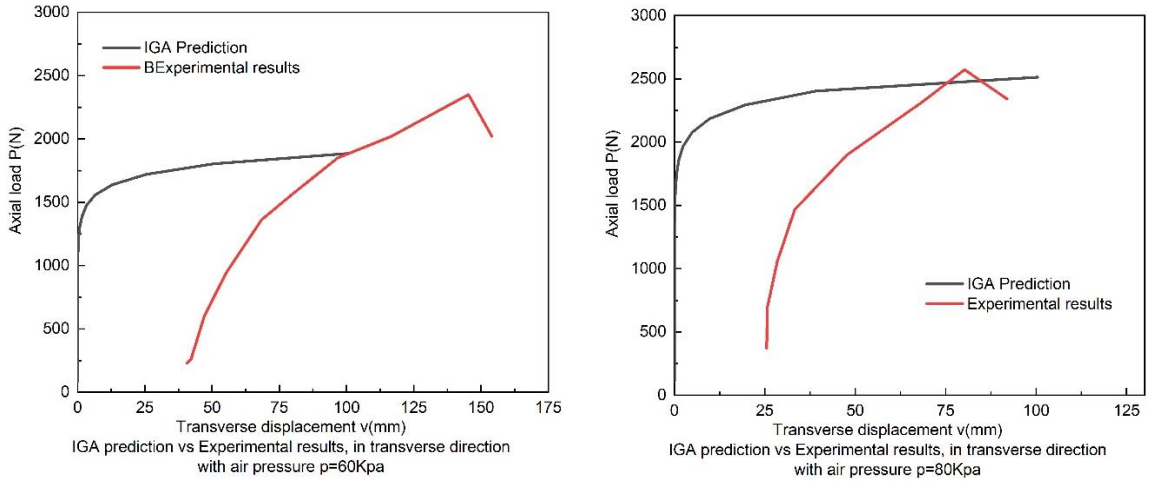

Figure 5.42 IGA prediction vs Experimental results, in transverse displacement v with air pressure 20 kpa, 40 kpa, 60 kpa and 80 kpa

5.8 Conclusion

An experimental program has been described in details which were the basis to carry out the buckling tests of HOWF inflatable beams. The experimental results were compared with numerical predictions based on isogeometric analysis performed with the Matlab code.

The experiment for determining buckling behaviour and load-carrying capacity of the inflatable composite fabric beams is conducted. Each beam is tested with four different air pressure magnitude. A test frame is constructed and the test has been successfully carried out.

The experimental results is used to calibrate the numerical model of inflatable beams to predict the buckling behaviour of the beam fabricated from orthogonal fibre laminated fabrics.

The objective of the experiment and acquisition data include:

- Determine the load-displacement relation of the inflatable beam with different air pressures.

- Determine the maximum load-carrying capacity of the inflatable beam with respect to the appearance of the first wrinkle.

Conclusions and further studies

1. Conclusions

Studying domestic and foreign methods then choosing isometric method as it is suitable with guide line of the researching topic.

Applying those methods to program the Matlap for the topic

Experimenting air beams and adjusting numerical models based on experimental results include:

+ Select suitable fabric to make air beams
+ Determinate material properties and design joints
+ Manufacture the air beams
+ Design instable examination of gas beam

Comparing experimental results with theoretical results then evaluating the selected method's suitability.

2. Further studies

The thesis has achieved certain results; however, there are still problems un-resolved which are selection of materials, air-beams producing, and measuring methods.

Therefore, the studied gas beams will be carried out with different shapes in future by selecting materials and fabricating beams with more uniformity. Besides, a measuring method is supposed more suitably, is that, using the camera to measure.

List of Publications

Parts of this dissertation have been published in international journals, national journals or presented in conferences. These papers are:

- **Articles in national scientific journal**

1. T. Le-Manh, Q. Huynh-Van, **Thu D. Phan**, Huan D. Phan, H. Nguyen-Xuan "Isogeometric nonlinear bending and buckling analysis of variable-thickness composite plate structures" Composite Structures 1 January 2017, Pages 818-826.

- **International Conference**

2. **Phan Thi Dang Thu**, Phan Dinh Huan and Nguyen Thanh Truong "Effect parametric to properties of a 2D orthogonal plain classical woven fabric composite"; ISBN: 978-604-913-367-1, pages 509-517.

- **National Conference**

3. **Phan Thi Dang Thu**, Phan Dinh Huan and Nguyen Thanh Truong "Biaxial beam inflation test on orthotropic fabric beam"; ISBN: 978-604-913-213-1, pages 1169-1176.

4. Nguyen Thanh Truong, Phan Dinh Huan, **Phan Thi Dang Thu** "Discretizing an analytical inflatable beam model by the shell-membrane finite elelment"; ISBN: 978-604-913-213-1, pages 1221-1228.

5. Phan **Thi Dang Thu**, Le Manh Tuan, Nguyen Xuan Hung, Nguyen Thanh Truong "Geometrically nonlinear behaviour of composite beams of variable fiber volume fraction in isogeometric analysis"; ISBN: 978-604-82-2028-0, Pages: 1404-1409.

6. **Thu Phan-Thi-Dang**, Tuan Le-Manh, Giang Le-Hieu, Truong Nguyen-Thanh "Buckling of cylindrical inflatable composite beams using isogeometric analysis"; ISBN: 978-604-73-3691-3, Pages 821-826.

7. **Phan Thi Dang Thu**, Nguyen Thanh Truong, Phan Dinh Huan "Mô hình dầm hơi composite phi tuyến chịu uốn"; ISBN: 976-604-82-2026-6, Page 699-706.

8. **Phan Thi Dang Thu**, Nguyen Thanh Truong, Phan Dinh Huan, Le Dinh Tuan "Biaxial experiments for determining material properties and joint strength of textile plain woven fabric composites"; ISBN: 978-604-913-722-8, Page 1174-11.